

THE X RAY DIAGNOSTICS  
OF THE ARGON FILLED DENSE PLASMA FOCUS

---

A Dissertation  
Presented to  
the Faculty of the Department of Physics  
University of Houston

---

In Partial Fulfillment  
of the Requirements for the Degree  
Doctor of Philosophy

---

by  
Pin-chieh Wang  
August 1976

## ACKNOWLEDGEMENTS

The author wishes to thank Dr. M. Eisner for many assistance during the experiment. He wishes also to thank his wife for the encouragement over the years and the assistance in drawing the figures of this work.

THE X RAY DIAGNOSTICS  
OF THE ARGON FILLED DENSE PLASMA FOCUS

---

An Abstract of a Dissertation  
Presented to  
the Faculty of the Department of Physics  
University of Houston

---

In Partial Fulfillment  
of the Requirements for the Degree  
Doctor of Philosophy

---

by  
Pin-chieh Wang  
August 1976

## ABSTRACT

An experimental investigation has been conducted to use a Dense Plasma Focus Machine as a prospected high intensity pulsed x ray source. The argon was chosen for the plasma discharge. An effort to reach the highest x ray intensity emission has been made. Although it has not yet been possible to operate with as high energy in argon as in hydrogen, the argon focus provides an intensified "point source" of x ray. Based on the diagnostic data and the characteristic difference between argon and hydrogen, a theoretical model of the shock wave was proposed. The x ray energy spectrum of the focus was determined by a crystal spectrometer. Analyzing this spectrum, one can obtain a combined radiation from a 3 keV thermal plasma and a 48 keV electron beam bombarding the center electrode. The polarization of the x ray was measured at a direction perpendicular to the DPF axis. The change of the polarization with time indicated that the plasma impinged radially and then followed by an axial flow. The correlation of the x ray signal with the voltage signal showed that the plasma resistance was rising after the density reached its maximum, and associated the increase of the resistivity as a result of the ion-acoustic instability.

## TABLE OF CONTENTS

	Page
I. INTRODUCTION . . . . .	1
II. THEORETICAL BACKGROUND . . . . .	9
2-0 Introduction. . . . .	9
2-1 Bernstein's Model . . . . .	9
2-2 Potter's Model. . . . .	11
2-3 Newman's Model. . . . .	13
2-4 Turbulence Investigation. . . . .	14
2-5 The Shock Wave. . . . .	17
III. EXPERIMENTAL METHODS . . . . .	19
3-0 Introduction. . . . .	19
3-1 Voltage and Current Measurements. . . . .	19
3-2 The Optimization of Operating Parameters for the DPF Filled with Argon . . . . .	25
3-3 X-Ray Detectors . . . . .	28
3-4 X-Ray Polarimeter . . . . .	34
3-5 Crystal Spectrometer. . . . .	39
IV. DISCUSSION OF EXPERIMENTAL RESULTS . . . . .	43
4-0 Introduction. . . . .	43
4-1 Voltage and Current Measurement . . . . .	43
4-2 Spatial and Temporal Studies. . . . .	47
4-3 Correlation Between the Voltage and X-Ray Signals . . . . .	66
4-4 Angular Distribution and Polarization of the X-Ray Emission. . . . .	70
4-5 X-Ray Spectrum Study. . . . .	80
4-6 Conclusion. . . . .	86
REFERENCES . . . . .	88

## CHAPTER 1

### INTRODUCTION

The Dense Plasma Focus was discovered in the early 60's, producing a very high density ( $n \geq 2 \times 10^{19} \text{ cm}^{-3}$ ) plasma of relatively long duration, high temperature (100-150 nsec for a few keV), and large neutron yield ( $10^{11}$  neutron per discharge).<sup>(1)</sup> Interest in the plasma focus has been generated by the fact that it reaches the value  $nt \approx 10^{12}$ , the closest value which has been achieved in laboratory plasmas to the Lawson's condition ( $nt \approx 10^{16}$ ) required for thermonuclear fusion. Here  $n$  is the number of particles per cubic centimeter and  $t$  is the time of confinement in seconds.

The plasma focus discharge was originally studied by Fillippov et al.<sup>(2)</sup> in the USSR and by Mather<sup>(3)</sup> in the U. S. A. in the early 1960. Early work in the U. S. A. with the coaxial gun system was pioneered by Marshall.<sup>(4)</sup> Mather following the work of Osher,<sup>(5)</sup> investigated the fast coaxial gun mode which led to the development of a higher pressure mode of operation. Fillippov et al, challenged by the problem of Z - pinch initiation along insulators, designed a metal wall-pinch apparatus to minimize or eliminate the influence of insulating walls on the pinch. The Russian and United States designs', although similar in many respects, still differ and the results were arrived at independently.

Figure 1-1-1 shows a typical diagram of the Mather type coaxial plasma focus apparatus for a 27 KJ, 20 KV condenser power supply used in

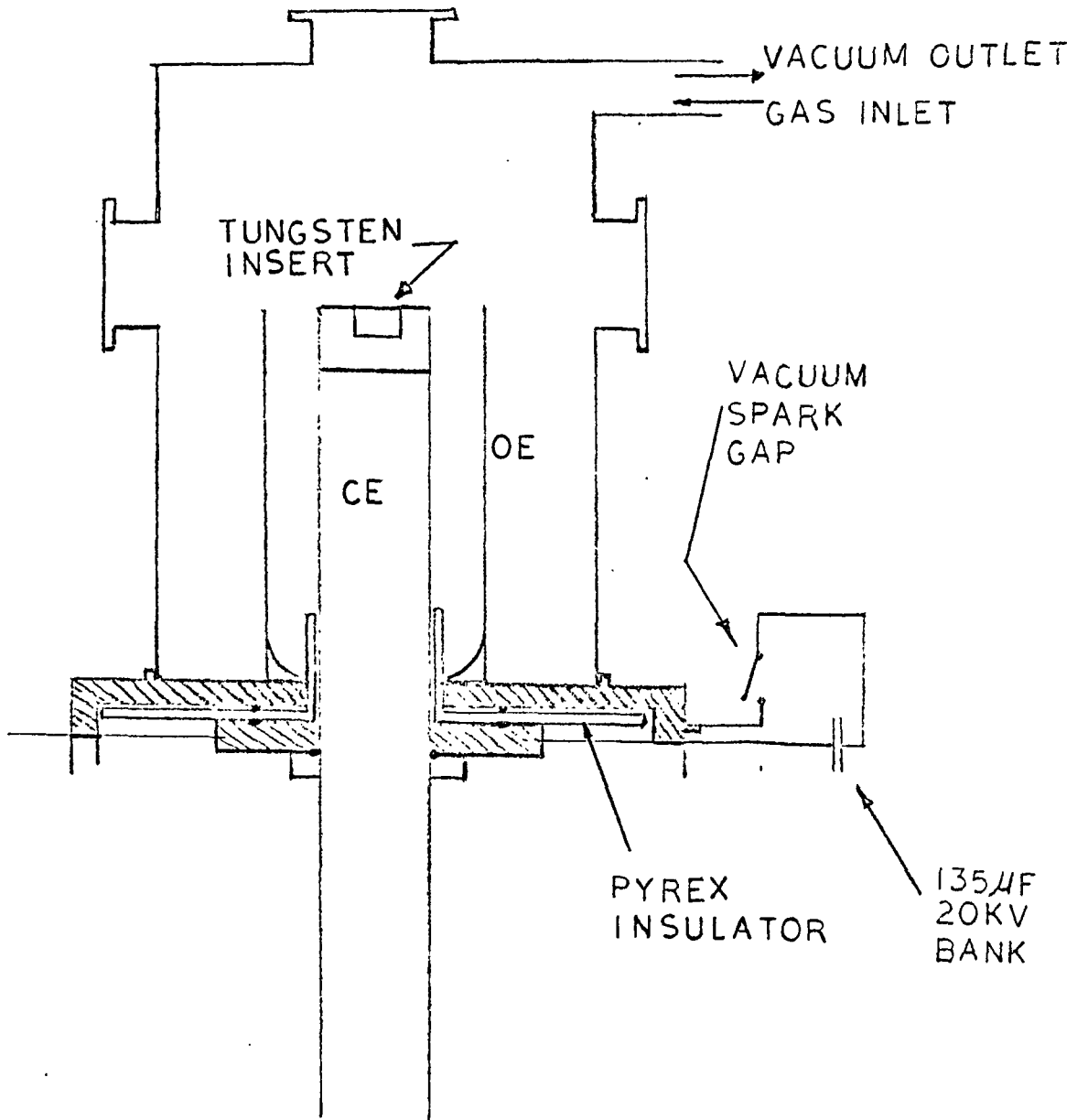


FIG 1-1-1 SCHEMATIC OF DPF MACHINE

the University of Houston. The design consists of two coaxial electrodes and a pyrex glass insulator across which the initial breakdown occurs. The outer electrode (OE) and center electrode (CE) diameters are 10 and 5 cm, respectively with a CE length of 17 cm for the hydrogen discharge. The CE diameter was kept unchanged while the OE diameter was reduced to 7 cm, and the CE length was reduced to 9 cm for the argon discharge. A small tungsten cylinder with diameter 2.5 cm was inserted into the front surface of the center electrode to reduce the erosion by electron bombardment during the final collapse. The OE is attached to a circular grounded aluminum cable header. The CE attaches to a central header that provides an electrical connection and vacuum seal. The hat-like pyrex glass insulator forms the vacuum seal between the CE header and the ground header. The central part of the insulator extends approximately 5 cm along the CE into the vacuum chamber. The energy storage bank consists of three identical modules (3, 15  $\mu\text{f}$ ) capacitors each of which is connected to the discharge header via a vacuum spark gap switch and eighteen low inductance coaxial cables.

The gas break down starts from the center positive electrode to the metal cathode back plate along the pyrex glass insulator within a fraction of a microsecond after the high voltage application.<sup>(1)</sup> As the discharge current increases a  $\vec{j} \times \vec{B}$  force perpendicular to the current sheath leads to radial and axial motion. The axial component of force  $\vec{j} \times \vec{B}$  varies as  $1/r^2$  across the annulus and leads to an axial sheath velocity that decreases with the radius thus, a parabolic shape current sheath is formed which propogates down the coaxial structure. This is the so called the run down stage of the plasma focus (see

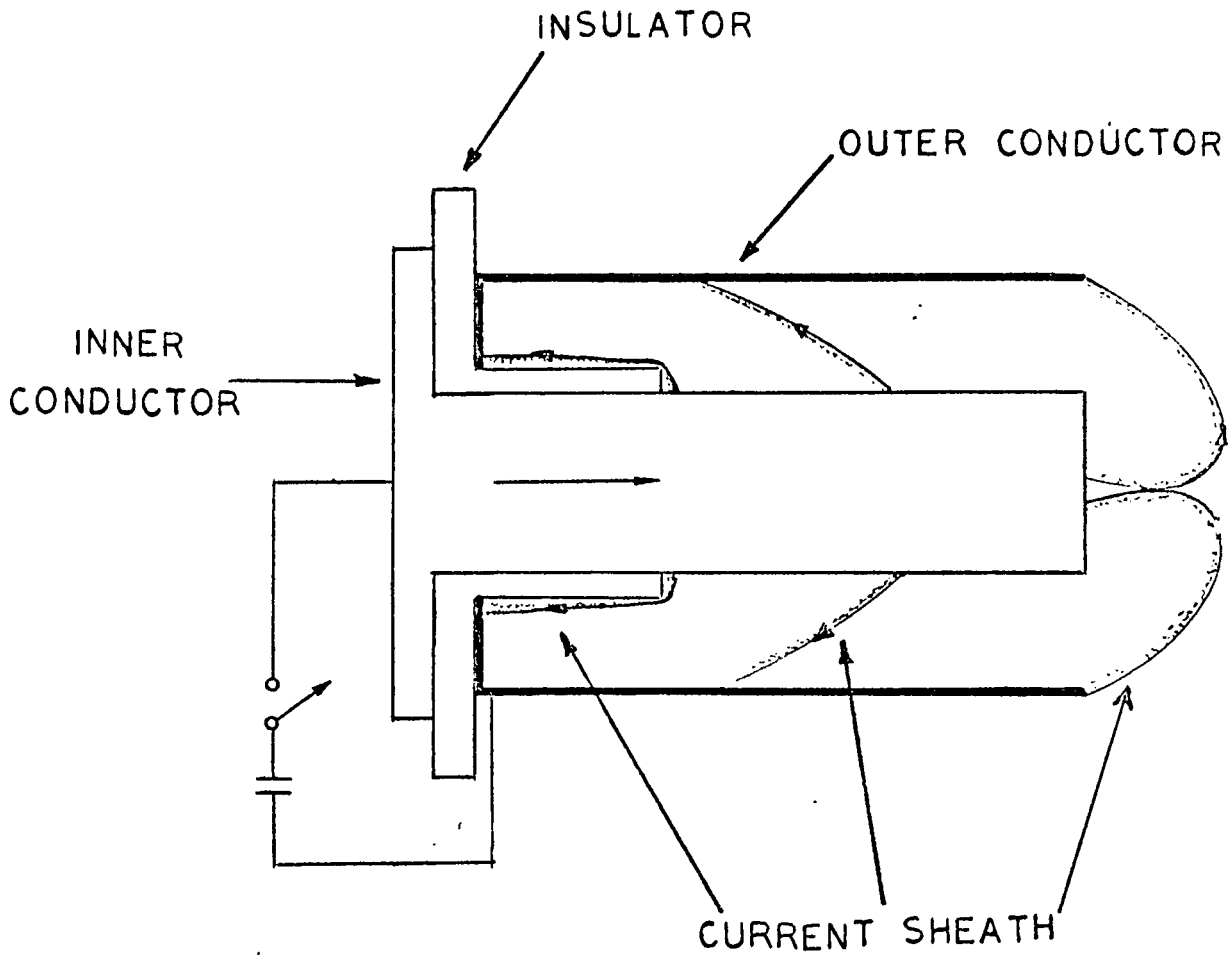


FIG 1-1-2 TIME DEVELOPMENT OF DPF  
CURRENT SHEATH

Figure 1-1-2).

The overall time for plasma sheath to travel to the end of the center electrode is related to both the applied voltage and the initial mass density of the filling gas. According to the "snowplow" model of Rosenbluth and Gerwin<sup>(6)</sup> the velocity of the current sheath is given by  $v_s = (c^2 E^2 / 4\pi \rho_0)^{1/4}$  cm/sec, where  $E$  and  $\rho_0$  are the applied electric field and the filling mass density respectively.

The current sheath arrival at the end of the center electrode is made to occur when the current is maximum by adjusting the length of the center electrode. Therefore, a large amount of the stored energy will be converted into the plasma focus.

The outer electrode initially chosen was a solid tube, but it was soon replaced by a squirrel cage. The squirrel cage allows the plasma flow to be pushed out of the magnetic field region so that the current sheath does not accelerate all the mass ahead of it. As a result, the focus can be operated at a higher pressure for the same driving current. Also, it was found that when squirrel cage outer electrode was used the current sheath arrival time at the end of the inner electrode was fairly insensitive to the filling pressure.

After the current sheath reaches the end of the accelerator, the plasma will undergo a rapid radial collapse off the end of the center electrode and convert part of the stored magnetic energy to plasma energy in the focus. The two dimensional  $r, z$  convergence is due to the  $\vec{j} \times \vec{B}$  pinch force. By the nature of the convergence 90% of the gas is ejected along the  $z$ -axis and lost. It is this fact that leads to a small final plasma radius and hence larger magnetic compression and

density than one would have obtained in a purely cylindrical collapse.

The focus duration is many times ( 10 times) greater than calculated from the  $m = 0$  magnetic hydrodynamic instability. It is<sup>(7)</sup> believed that the stabilization of the  $m = 0$  mode is the result of high velocity axial gas flow along the focus column. In the deuterium discharge the pinch column lasts for approximately 60 nsec. During the focus state, the average density is estimated to be  $n_e \sim 6 \times 10^{18} \text{ cm}^{-3}$ , with the peak density approximately  $4 \times 10^{19} \text{ cm}^{-3}$  in the most highly pinched regions. After the dense pinch breaks up, a less dense plasma forms with density approximately  $10^{18} \text{ cm}^{-3}$ . In the low density phase a higher temperature plasma is generated by a turbulent mechanism.<sup>(8)</sup> A hard x-ray emission and an enhanced neutron flux are observed at this stage.

The stability of the focus column can be greatly increased by adding a small d.c. axial magnetic field. With the magnetic field, the heating mechanism for ions and electrons is inhibited, as expected. Due to a trapped magnetic field, the spatial stability of the focused column offers a great possibility for scaling to higher energy. A hollow center electrode was first used by Prior<sup>(9)</sup> to eliminate the x-ray's arising from anode bombardment by electrons. He found that use of the hollow electrode did not alter the focus emission significantly. However, the voltage profile shows only one spike during the collapse as opposed to multiple spikes seen with the solid anode. It was explained that the focus is formed closer to the electrode and more symmetric pinch collapse can be formed in the hollow electrode.

The dynamics of the plasmas focus has been studied theoretically by the computer simulation. Potter has developed a 2-dimensional, two

fluid numerical simulation code to describe the focus. Although density, temperature, and the life time of the focus discharge have been well predicted, the following hard X-Ray emission and low density stage is not obtained, and the anisotropy in space of the neutron yield does not agree with the observation.

It is not clear that a fluid model can adequately describe all the properties of the focus, and there are always arguments between the two contradictory mechanisms; namely, the thermal plasma suggested by the soft x-ray emission, and the plasma turbulence suggested by the hard x-ray and the neutron yields.

Based on x-ray pinhole pictures, the hydrogen plasma has typical dimension of 1.5 mm in radius and is 2.5 cm long. The plasma volume contains approximately 15 Joule of energy and is a copious source of X-rays. (11)

The x-rays generated from DPF originate from the plasma bremsstrahlung, recombination radiation and the electron bombardment of the electrode surface. The intensity of the bremsstrahlung is proportional to  $Z$ , the charge of the plasma ions. It is our purpose therefore to study the characteristics of the DPF machine filled with a high  $Z$  gas, in our case argon was chosen, to achieve a higher x-ray yield. Along with the increase in x-ray yield, the plasma may be expected to behave differently since the increase of the mass of the atom will reduce the rate development of many plasma instabilities.

Primarily, x-ray diagnostic methods were used to study the argon plasma focus. The x-ray measurements included spatial and temporal measurements, the polarization investigation and the determination of the

spectrum.

In the second chapter, a summary of the recent theoretical models for the development of the hydrogen focus is given. In the third chapter, the experimental method is described. This includes the preliminary study for the operating parameters for the plasma focus in argon, the design of both the x-ray polarimeter and the x-ray spectrometer. In the last chapter, the experimental data is presented and analyzed.

## CHAPTER 2

### THEORETICAL BACKGROUND

#### 2-0 Introduction

The laboratory observation of the focus stage of DPF drawing the attention of plasma physicists are: (1) The hard x-rays emitted from the plasma focus are approximately 50 nsec after the collapse on the axis. (2) The emitted neutrons showed an average energy shift of up to 500 keV with respect to the center of mass energy. (3) The lifetime of the plasma focus in hydrogen is 50~100 nsec., a value approximately ten times longer than the theoretically predicted value.

To explain these phenomena two modes of plasma dynamics have been considered initially: a beam-target model and a "moving boiler" model. The measured characteristics of the emitted neutrons and x-rays from various plasma focus devices indicate that neither model adequately explains the observed behaviour.<sup>(12)</sup> In this chapter a brief summary of the recent theories about the dynamics of the focus stage is given, and a simple model of the magnetic driving shock wave is explained.

#### 2-1 Bernstein's Model

In 1960 Bernstein<sup>(13)</sup> used computer techniques to apply the Z pinch discharge theory to the plasma focus. He calculated the ion trajectories in the crossed electric and magnetic fields generated by a rapidly

collapsing current distribution.

Instead of computing the plasma dynamics in a completely self-consistent manner, Bernstein assumed an axial current distribution

$j_z(r, t)$ , which is finite in thickness and initially annular in shape. This current distribution is then assumed to contract rapidly to the axis. During the time of the contraction both an azimuthal magnetic field  $B_\theta(r, t)$  and an axial electric field  $E_z(r, t)$  are produced.

The Maxwell's equations are:

$$\frac{\partial(r B_\theta)}{\partial r} = r j(r, t) ; \quad \frac{\partial E_z}{\partial r} = \frac{\partial B_\theta}{\partial t} \quad (2-1-1)$$

for the symmetric geometry.

The current density assumed by Bernstein is given by the equation:

$$j(r, R) = j_a + (j_b - j_a) \left( \frac{r}{R} \right)^\alpha \quad (2-1-2)$$

where  $R$  is the boundary radius of the current sheath which is time dependent via the boundary velocity  $dR/dt$ ,  $j_a$  is the current density on the axis,  $j_b$  is the current density at the boundary  $R$ , and  $\alpha$  is a positive constant.

Both  $j_a$  and  $j_b$  varied with time in a way consistent with the total discharge current, which was assumed to remain constant during the time of interest. The boundary was assumed to contract at a uniform rate  $dR/dt = -V_b$  and the value of  $\alpha$  was chosen in the range from 0.3 to 3.0.

In addition to the above assumptions, one characteristic was also implied from the axial symmetry of the system; that is, the values of both the electric and magnetic fields vanish on the axis for all time, and

the ratio of the fields  $E_z/B_0$  varies as  $r/R$  to a first approximation.

From the above assumptions, the two fields can be calculated as a function of time, and two kinds of ion orbits are obtained. The ions making up the first kind of trajectory never reach the axis but gradually drift against the electric field in the  $\vec{B} \times \vec{v}/|B|$  direction. The ions of the second class oscillate through the axis and exhibit a pronounced movement in the direction of the electric field. Based on Bernstein's calculation, the second type of ion can be accelerated up to energies 100 times higher than their initial value.

This theory can explain neutron production fairly well, but cannot explain its energy shift with respect to the center of mass energy.

In 1973, Gary and Hohl<sup>(14)</sup> published a modified version of the Bernstein theory with the following three differences: (1) The particles were considered to have an initial spatial distribution as well as a Maxwellian initial velocity distribution. (2) The ion trajectories were calculated in 3-dimensional configuration space. (3)  $E_z$  was assumed to vanish outside the plasma. This assumption implies a strong induced electric field on the axis leading, in the case of a decreasing current, to strong ion acceleration in the direction of current flow.

Based on the above assumption, Gary and Hohl found that their model can accelerate the ions more efficiently than the Bernstein's model and they conclude that strong ion acceleration away from the anode occurs, not during the collapse phase, but during the focus phase.

## 2-2 Potter's Model

In 1973, D. E. Potter<sup>(10)</sup> developed another computer simulation of

the focus, using a fluid model, he approached the final pinch with a different heating mechanism. Instead of calculating the acceleration of a single ion, he considered three different mechanisms for ion heating: adiabatic compression, viscous heating, and joule heating, which are caused by adiabatic implosion, resistivity and viscosity respectively. Due to the axial velocity component in the imploding shock acting as a sink to remove the snowplowed plasma, the density in the imploding shock remains relatively low. The adiabatic heating is given by the formula

$$T_f/T_i = (\rho_f / \rho_i)^{\gamma-1} \quad . \quad \text{For deuterium } \gamma = 5/3$$

and the density increased by a factor of 20 (shock to pinch) so we have

$$T_f = 7.4 \times T_i \quad \text{The electron temperature in the shock is}$$

increased by Joule heating and with the subsequent compression on the axis, adiabatic compression can raise the electron temperature to 1.1 keV. On the other hand, the ion temperature at the imploding shock is approximately 30 e.v., and thus adiabatic compression alone can raise the ion temperature to the order of 200 e.v. However, with increasing temperature, the ion mean free path is increased and the ion viscosity becomes increasingly important. The ion viscous heating can then raise the temperature to the order of a Kilo-volt.

The closed set equations used in Potter's fluid model are as following:

$$\text{Conservation of mass:} \quad \frac{\partial \rho}{\partial t} + \nabla \cdot \rho \mathbf{v} = 0 \quad (2-2-1)$$

$$\text{Conservation of Momentum} \quad \frac{\partial \rho \vec{v}}{\partial t} + \nabla \cdot (\rho \vec{v} \vec{v} + p \vec{I} + \vec{\tau}) - \vec{j} \times \vec{B} = 0 \quad (2-2-2)$$

$$\text{Conservation of magnetic flux:} \quad \frac{\partial \vec{B}}{\partial t} = -\vec{\nabla} \times \vec{E} \quad (2-2-3)$$

Conservation of energy: 
$$\frac{\partial(p\epsilon)}{\partial t} + p \nabla \cdot \vec{V} + \nabla \cdot (p\epsilon \vec{V} + q) = \eta j^2 - p \frac{(\epsilon_e - \epsilon_i)}{\tau_{ei}} - p \quad (2-2-4)$$

where  $\eta$  is the resistivity,  $p$  is the power lost due to the bremsstrahlung radiation. It was assumed that the system displayed cylindrical symmetry, therefore, a 2-dimensional plasma simulation is allowed. During the focus state the ion-ion collision time  $\tau_{ii} \approx 20$  nsec. is of the same order magnitude as the macroscopic time scale of the focus itself, and thus the conditions for the fluid approximation are only partially fulfilled.

The important feature observed in this simulation is the long lifetime of the plasma pinch, although hydromagnetic instability would be expected to break it up in time 10 nsec. It has been concluded in this paper that the MHD instability is stabilized by the finite Larmor radius effects.

The neutron production calculated from the hot thermal pinch zone is slightly low, but is within its uncertainty limit.

### 2-3 Newman's Model

In 1975, a different view point of the electron heating mechanism in the production of the hard x-ray was published by Newman and Petrosian.<sup>(15)</sup> They pointed out that the boundary condition assumed by Bernstein as  $E = 0$  at  $r = 0$  was not justified. Instead, from the constant potential difference between the electrodes and the fact that

$\nabla \times E = 0$ , they claimed that the integral  $\int_{CE}^{OE} \vec{E} \cdot d\vec{l} = V_0$ . Where  $V_0$  is the applied voltage, CE and OE represent the center

electrode and outer electrode respectively. Then considering the fields on the two surfaces of the current sheath, they obtained the relation

$$E^B - E^A = \frac{\vec{v}}{c} \times \vec{B} \quad .$$

Where  $E^B$  and  $E^A$  are the electric fields inside and outside of the plasma column respectively. Based on the experimental observation and the value of  $E^B - E^A = -400 \text{ KV/cm}$  they claimed a strong electric field can be generated at the final collapse stage on the axis. They believed that this axial electric field is strong enough to accelerate the electrons to a few hundred kilovolts within approximately 5 nsec. These relativistic electrons are accelerated away from the center electrode, generating the hard x-rays from electron, duetron encounters. However, they accepted Gary and Hohl's model of ion acceleration. In this model the energetic ions are accelerated by  $dI/dt$ , instead of the motion of the current sheet. Thus, acceleration of electrons and the production of hard x-rays occurs during the last few nanoseconds of the collapse phase. While the ion acceleration and neutron production takes place at the beginning of the focus phase when the weaker field (produced by  $dI/dt$ ) is the only one present. The extremely short time interval between these two events could then account for the apparent coincidence of the onset of the neutron and hard x-ray pulses.

#### 2-4 Turbulence Investigation

The turbulent theory of the plasma focus was originated from the observation that the greatest number of neutrons are emitted some time (50 nsec) after the collapse on the axis. Based on this phenomenon Maisonnier<sup>(8)</sup> proposed the following heating mechanism. The dense plasma column at maximum compression (see Figure 2-4-a), is disrupted by

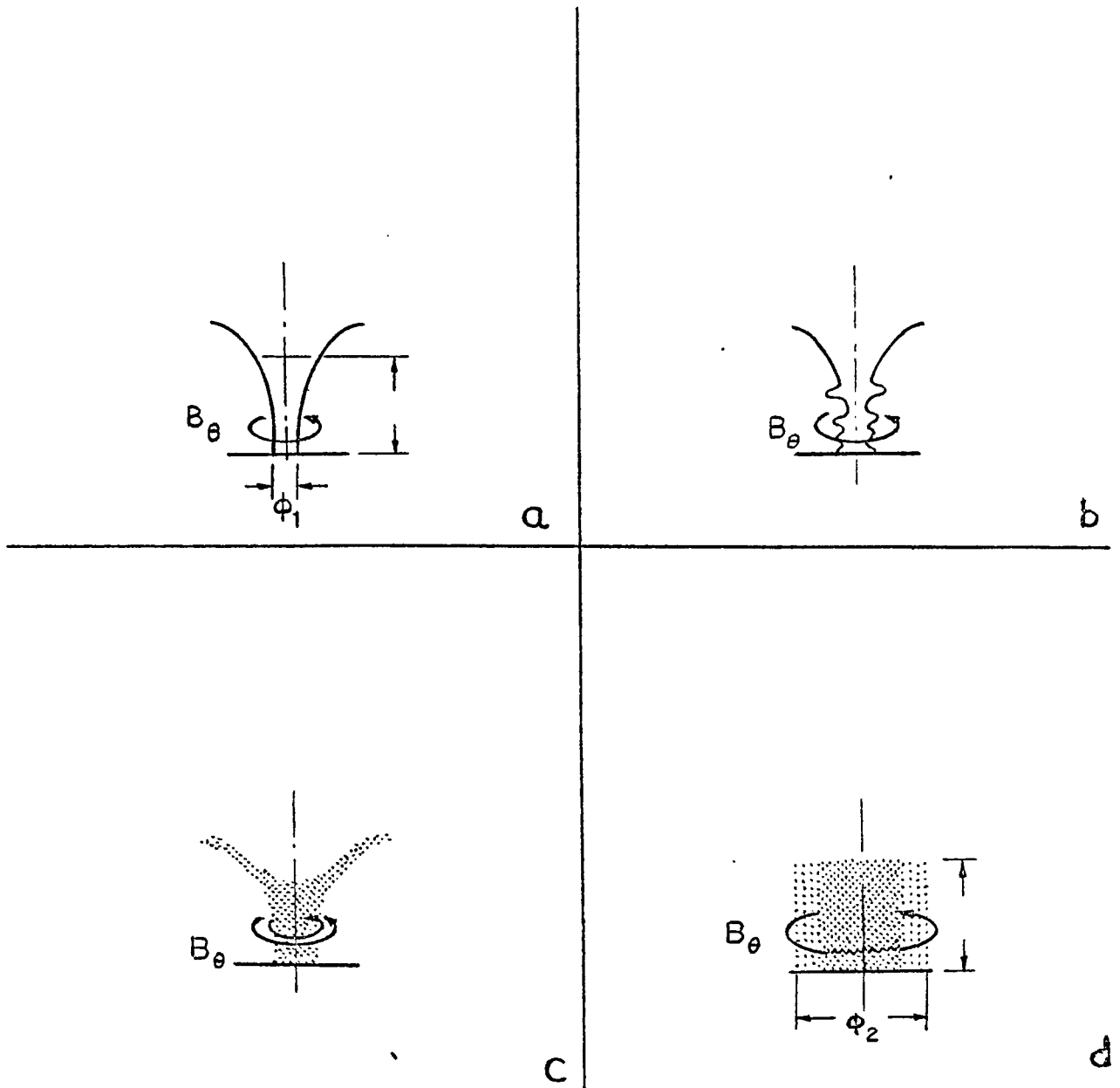


FIG 2-4 TIME DEVELOPMENT OF DPF  
AFTER MAXIMUM COMPRESSION

macroscopic  $m = 0$  instability (See Figure 2-4-b). The radial extension of the plasma increases, density goes down, and the magnetic field is mixed up with the plasma, and the dark pause period is formed (See Figure 2-4-c). During the time the plasma column stores internally the magnetic energy which was present in the vicinity of the pinch, the resistivity is so low that this energy is not converted appreciably into the thermal energy. At some radius of expansion, the conditions for onset of turbulent heating are satisfied (Figure 2-4-d); the magnetic energy stored in the plasma is transformed into thermal energy, and a second burst of neutrons and x-rays is obtained.

It is well known (from MHD calculations) that the Bennett relation holds at the instant of collapse.

$$I^2 = 4 N K T \quad (2-4-1)$$

There is also evidence that current carrying column keeps contracting or at least does not expand immediately after collapse whereas the plasma radius  $r$  increases,<sup>(16)</sup> and that the current  $I$  remains roughly constant during the whole neutron emission. If  $\alpha r$  is the radius within which the current is contained, ( $\alpha < 1$ ). Then, assuming that the plasma density is constant across  $r$ , the current is given by  $I = \alpha^2 N e V_d$ , where  $V_d$  is the drift velocity of the electrons.

Thus we obtain:

$$\alpha^4 N = \frac{4}{3} \frac{m_e}{e^2} \left( \frac{V_{the}}{V_d} \right)^2 = 5 \times 10^{12} \left( \frac{V_{the}}{V_d} \right)^2 \quad (2-4-2)$$

The ion-acoustic instability could occur when the condition  $V_d / V_{the} \geq (m_e / m_i)^{1/2}$  is satisfied, and this implies that  $\alpha^4 N \leq 2 \cdot 10^{16}$

and, as  $N \approx 2 \cdot 10^{18}$ , the condition  $\alpha < \frac{1}{3}$  is obtained. Then when the radius of the plasma column reaches about 3 times the radius at maximum compression, ion acoustic instabilities could be developed. The imaginary part of the frequency  $I_m(\omega)$  would be conveniently large ( $10^{10}$  per second) and the resistivity is high enough to justify the heating of  $2N$  particles per cm height of plasma column to a few keV in less than 100 nsec.

## 2-5 The Shock Wave

To consider the structure of the shock wave during the run down stage, we can use the following physical model. After approximately one  $\mu$ sec after the initial breakdown, the plasma reaches an equilibrium stage. A strong magnetic field is generated by the current flowing along the central electrode. This magnetic field drives the plasma in the outward direction. As the plasma penetrates into the surface layer of the magnetic field, the particles will essentially move along the cyclotron orbit. Since the ions have a much larger radius of gyration than the electrons, they will tend to penetrate further into the region of the magnetic field. This creates a space charge and an electric field. Based on the experimental result, the resistivity for plasma is so small that a very small electric field will generate the current density. It is therefore necessary that the electric and magnetic fields must adjust themselves in such a way that  $\vec{E} + \frac{\vec{V} \times \vec{B}}{c} \approx 0$ . The characteristic thickness of the shock wave can be calculated from the self-consistent dynamic equations and is given as  $\delta \sim (m/4\pi N e^2)^{1/2}$ . From this relationship if we change the discharge gas from hydrogen to

argon the shock thickness will increase by a factor of approximately 6.

From the experimental observations the current sheath travels along the electrode with an average velocity of approximately 8 cm/ $\mu$ sec.

under the condition of  $P_0 = 3 \text{ Torr}$ ,  $V_0 = 20 \text{ kV}$  for the hydrogen discharge. While the velocity of the sound wave under the same condition can be calculated from the formula  $C_s = (\gamma P / \rho)^{1/2}$ .

For the hydrogen plasma  $C_s \sim 12.7 \times 10^4 \text{ cm/sec}$  at electron temperature  $T_e \sim 30 \text{ eV}$ , one concludes that the current sheath is supersonic.

If we assume the mass density is constant along the current sheath. the velocity of the current sheath close to the central electrode is greater than the sheath velocity close to the outer electrode because the magnetic force is proportional to  $1/r^2$ . Thus, the current sheath leans further backward as the sheath travels down the electrode. Since the diffusion coefficient is smaller<sup>(18)</sup> for a strong magnetic field the thickness of the shock wave will gradually increase with increasing radius.

## CHAPTER 3

### EXPERIMENTAL METHODS

#### 3-0 Introduction

In this chapter we introduce the instruments used in our experiments and the theories on which our designs were based. These instruments include the voltage and current probes, the x-ray polarimeter, and the x-ray spectrometer.

The characteristics of the x-ray detectors are presented. The range of operation of the DPF in Argon is discussed and the operating parameters for our experimental studies are determined.

#### 3-1 Voltage and Current Measurements

Voltage and current probes whose output is displayed on an oscilloscope can reveal significant features of transient gas discharges, such as those occurring in the DPF device. In this study the information provided by the voltage and current probe is used to select the optimum operating parameters. The voltage probe consists of a voltage divider which is connected between the center and outer electrodes. The current is measured from the integrated signal of the output of a Rogowsky loop coupled to one of the bank capacitors. The configuration of these two probes and typical output traces obtained for the DPF operating with hydrogen are shown respectively in Figure 3-1-1 and Figures 3-1-2.

Since the inductance of the machine varies considerably during the

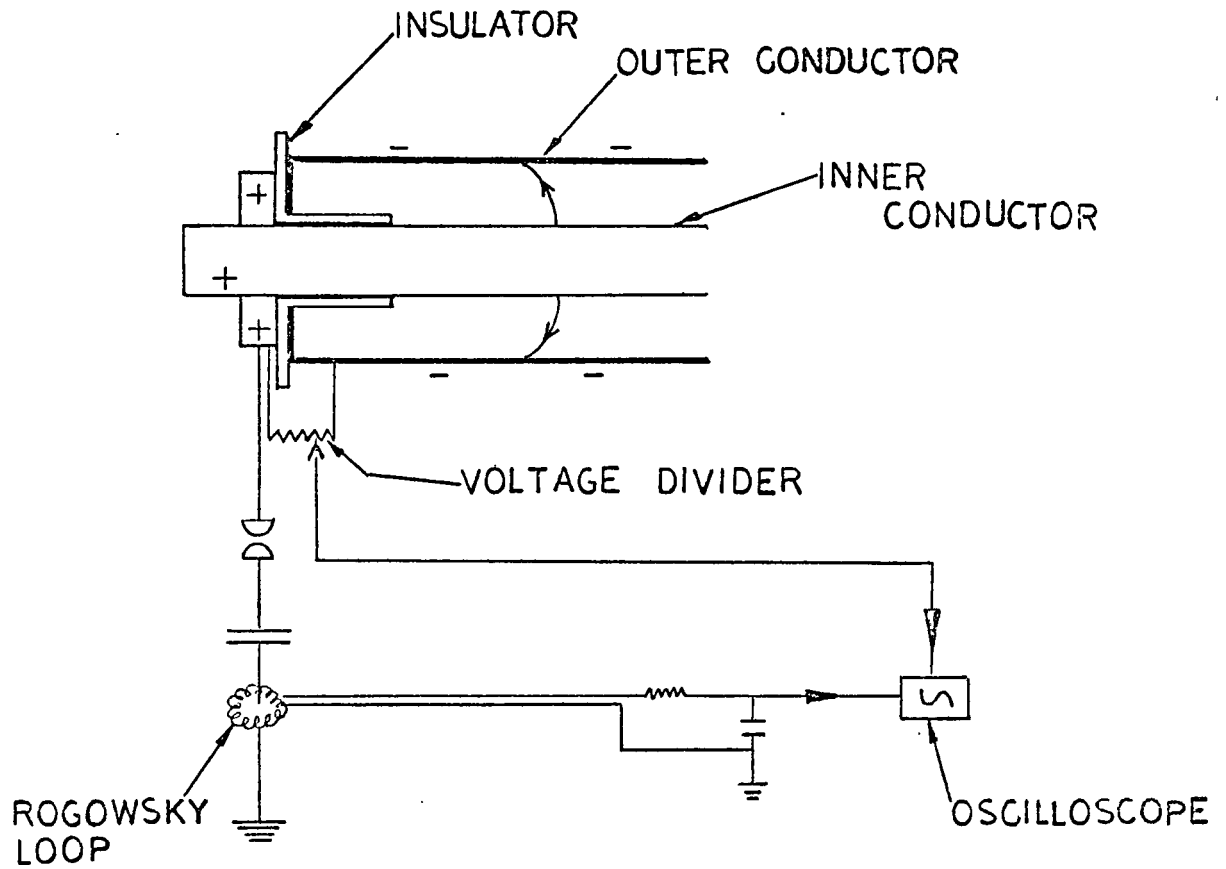


FIG 3-1-1 VOLTAGE AND CURRENT PROBES IN DPF

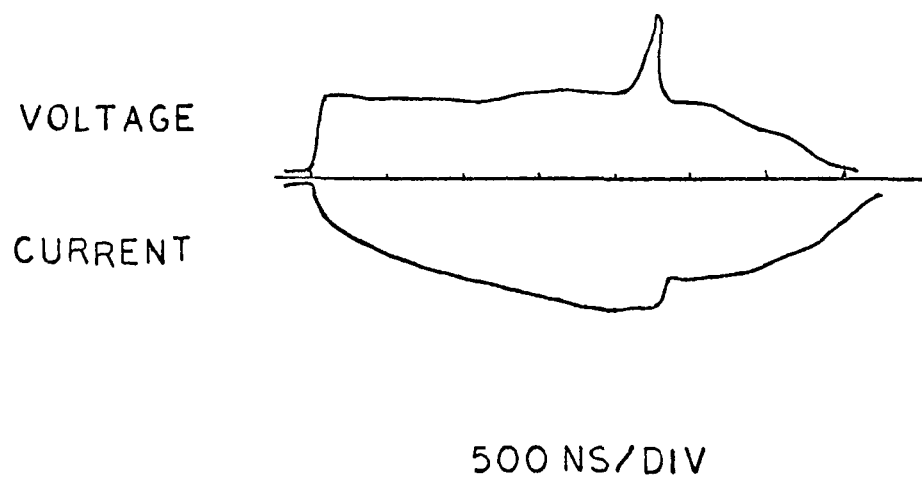


FIG 3-1-2 VOLTAGE AND CURRENT  
TRACES OF HYDROGEN FOCUS

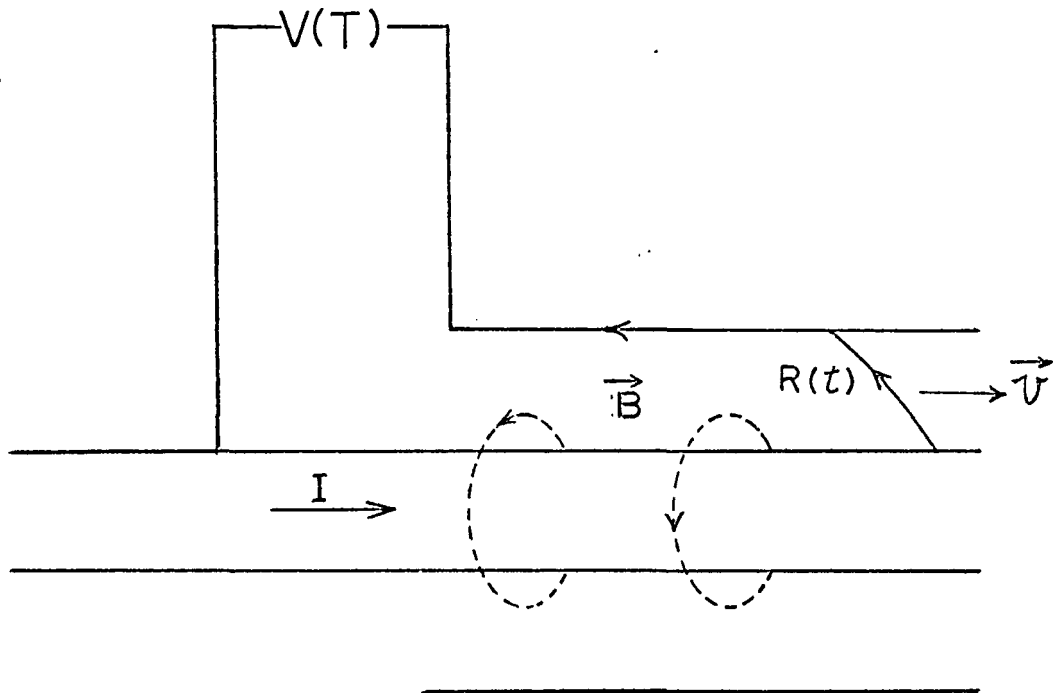


FIG 3-1-3 ILLUSTRATION OF THE  
INDUCTANCE VARIATION IN DPF

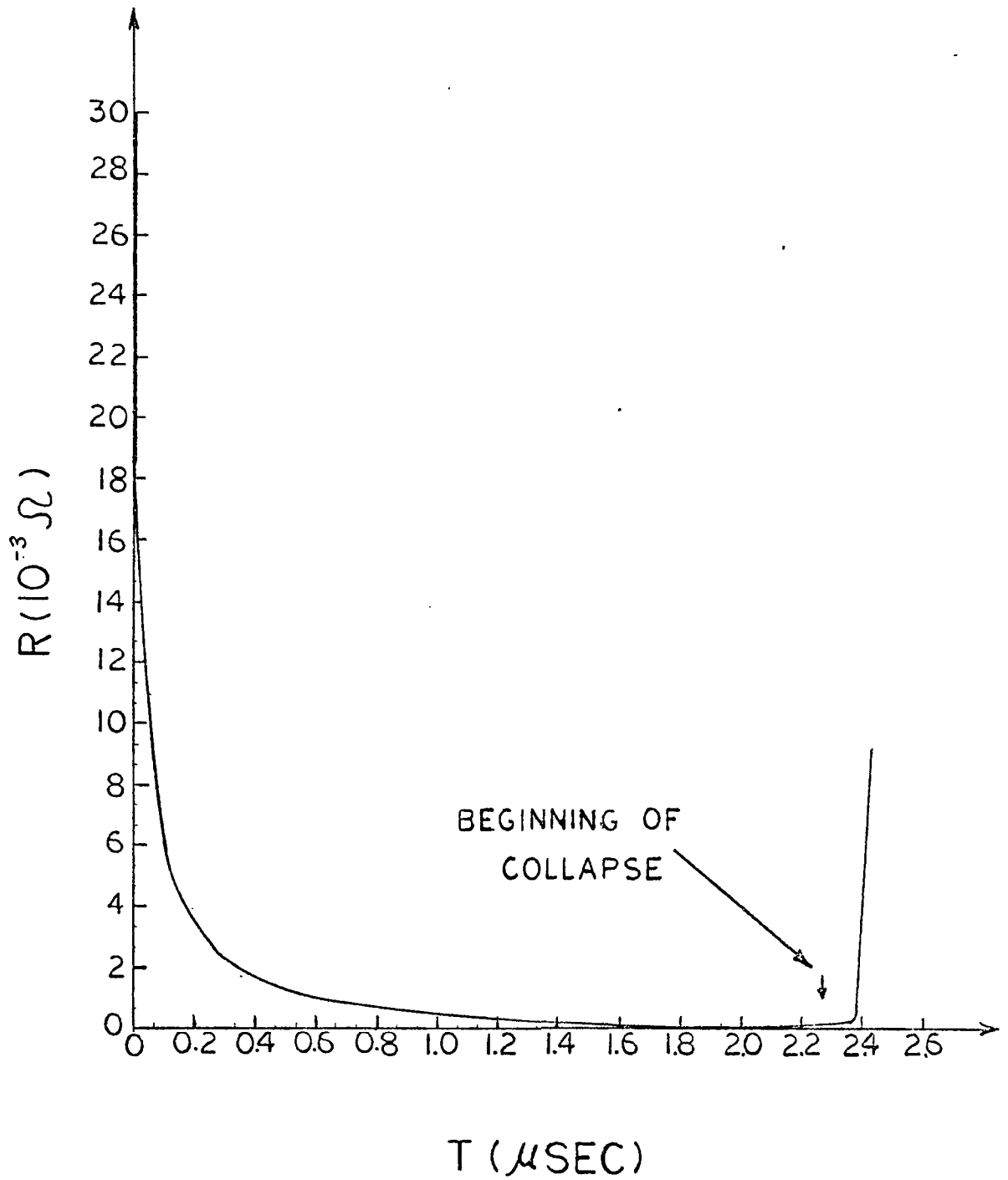


FIG 3-1-4 DPF CURRENT SHEATH RESISTANCE  
AS A FUNCTION OF TIME

discharge, the voltage actually measured is the sum of the induced voltage and the ohmic voltage<sup>(1)</sup> (see Figure 3-1-3).

$$V(t) = \frac{d}{dt} [L(t) \cdot I(t)] + I(t) R(t) \quad (3-1-1)$$

Where  $V(t)$  is the measured voltage,  $L(t)$  is the inductance of the system,  $I(t)$  is the total current and  $R(t)$  is the plasma resistance.

The resistance variation has been measured by Mather<sup>(1)</sup> (see Figure 3-1-4). Typically, approximately 1  $\mu$ sec after the initial breakdown, the resistance of the plasma drops below  $10^{-3}$  ohms. Since the magnitude of the current during the rundown stage is of the order 500 KA, the resistance contribution to the voltage is only about 500 volts. On the other hand, as seen from Figure 3-1-2 the measured voltage is more or less constant during the rundown stage, having a value about the same as the bank charging voltage, some tens of kilovolts. It is therefore reasonable to ignore the second term in eq. (3-1-1) which becomes:

$$V(t) = \dot{L}(t) I(t) + L(t) \dot{I}(t) \quad (3-1-2)$$

For the discharge of hydrogen, the voltage remains approximately constant during the run down stage, indicating that the two terms  $\dot{L} I$  and  $L \dot{I}$  in eq. (3-2) balance each other. In addition, the experimental evidence shows that the current sheath travels at a constant speed while the current magnitude displays sinusoidal behavior, increasing to a maximum value just before the final collapse. This implies that  $L(t)$  is increasingly linearly while at the same time  $\dot{I}(t)$  decreases to zero.

The voltage trace after the constant rundown stage is characterized

by a sharp spike rising to approximately 40 KV. This spike is generated because of the large change in the inductance of the sheath during collapse. After collapse the voltage decreases gradually.

The current varies sinusoidally, and is characterized by the time  $\tau = (LC)^{1/2}$ , however, there is a sudden decrease associated with the final collapse. This sudden decrease is caused by a strong induced  $\vec{v} \times \vec{B}$  field whose direction is opposite to that of the field produced by the capacitor bank. In general, the feature of the probe signal described here, can serve as useful indicators of the nature of the focus formed. Large single voltage spike and large sudden current decrease are taken to be indication of a collapse to a high density, well formed focus. The formation of a focus with gases other than hydrogen will in general give different traces, but they will still provide useful diagnostic information.

### 3-2 The Optimization of Operating Parameters for the DPF Filled with Argon

The operation of the DPF machine has been extensively studied for hydrogen, deuterium and helium filling gases. Although argon has been added as an impurity in hydrogen discharge, there has been no work reported on the exclusive operation with heavier gases such as argon. Initially, the geometrical configuration of the electrode used for argon discharge was the same as for hydrogen.

The first phenomenon observed was that in argon discharge the time from the initial breakdown to the final pinch is about 3 times longer than that for hydrogen. Since the sheath travels more slowly the final collapse occurred considerably after the current had peaked.

The slower velocity of the sheath is expected since the mass of argon is considerably greater than that of hydrogen. After estimating the delay time, we reduced the electrode length from 15 cm to 9 cm in order to have the final collapse occurring at current maximum. When this shorter electrode was used, the current sheath reached the end of the electrode when the current was maximum.

The magnitude of the peak current in the PDF is largely determined by the ratio  $\dot{L}/R_c$ , where  $R_c \equiv 2(L/c)^{1/2}$ . Since the argon current sheath travels at a slower speed than hydrogen  $\dot{L}$  is less than that for hydrogen. To increase the current the outside electrode was replaced with a smaller one reducing the value of  $R_c$ . An electrode with a diameter of 7 cm was available and found to be satisfactory. Various capacitors combination were investigated; the two capacitor bank discharge gave the highest voltage spike. Although many other variations were tried unsuccessfully to obtain operation at higher energy, the electrode structure and charging capacitors described here gave the most reliable operation and was used for the bulk of the experimental studies.

A systematic investigation was carried out to determine the range of operating parameters for this configuration of electrodes and its associated banks. We found that the focus could be formed only in a limited domain of parameters [See figure (3-2)]. This is in sharp contrast to the wide range available for the operation of the hydrogen discharge.

The highest bank voltage for which a good focus was achieved was 12 KV. Using this voltage, the filling pressure was limited to be in

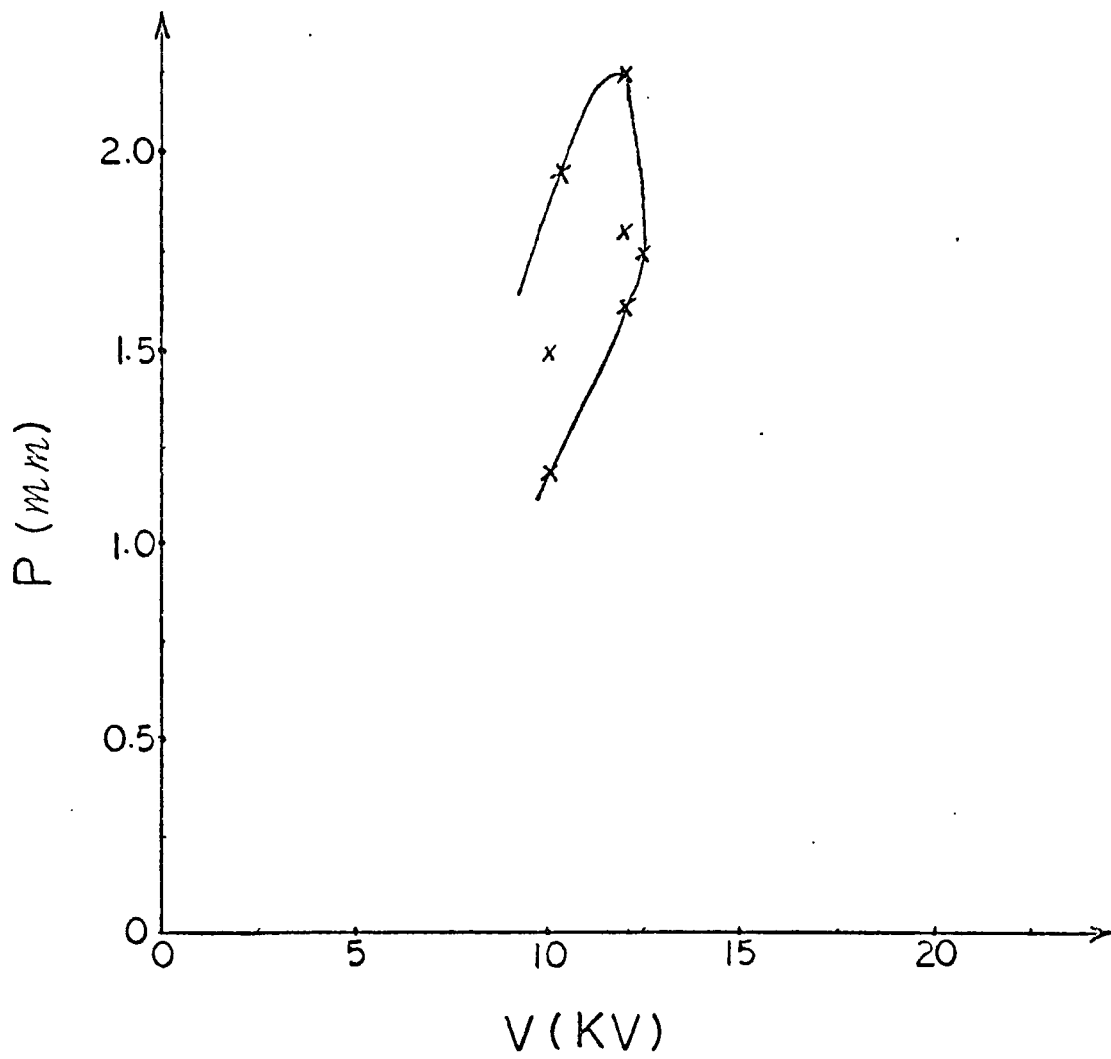


FIG 3-2 ARGON DPF OPERATING DOMAIN

between 1.6 mm and 2.2 mm with the best focus formation observed at 1.8 mm pressure. Therefore we chose 12 KV as the bank voltage and 1.8 mm as the chamber pressure for all of the experiments. With these parameters the voltage spikes as high as 27 KV were observed.

In the course of our systematic examination of the operating parameters, we also found out that approximately 10 to 15 shots were required to condition the discharge chamber after the electrode was exposed to air. Both the solid and hollow center electrode were used. Although a good focus seemed to be obtained with both, the solid electrode was chosen for the bulk of the work.

### 3-3 X-Ray Detectors

Two types of x-ray detectors were used during the x-ray studies of the DPF machine; namely, a photomultiplier x-ray detector and a solid state PIN detector. The photomultiplier detector consists of a RCA 931A photomultiplier coupled to a NE102 scintillator. An x-ray bandpass filter developed by Bernstein was built, and placed between the photomultiplier of the x-ray window.

The x-ray bandpass interval is formed by a combination of the transmission through the Titanium filter and the absorption in the thin sheet of the scintillation plastic.<sup>(19)</sup> The thickness of the scintillator is chosen to transmit the high energy signal while the thickness of the titanium filter is chosen to shield out the low energy x-rays.

The energy dependent response  $R$  of the detector is determined by the relation  $R = TA$ , where  $T = \exp(-\mu_f t_f)$  is the fraction of the X-rays transmitted through the titanium foil, and  $A = 1 - \exp(-\mu_s t_s)$  is the

fraction of the x-ray absorbed by the scintillator. Here  $\mu$  and  $t$  are the photoelectric absorption coefficient and material thickness respectively. From the thickness and the material chosen we can determine the energy and width of the bandpass. It is clear that when both the filter and the scintillator are chosen thinner, the bandpass interval will move to lower photon energies.

For the argon discharge, the dominant radiation from the plasma focus was observed to be around 3 keV, or slightly lower. It was therefore necessary to design a filter having the highest response in the vicinity of this energy region.

Table 3-3-1 shows the relative absorption intensity of NE102 for 0.01 cm and 0.005 cm thickness, while Table 3-3-2 shows the relative transmission for titanium at  $5 \times 10^{-4}$  cm and  $5 \times 10^{-3}$  cm thickness for the same energy range. Figure 3-3-1 shows the product of  $T_{Ti}$  and  $A_{NE102}$ . Curve a is the composition of  $T_1$  and  $A_1$ , while curve b is the composition of  $A_2$  and  $T_2$ . The b curve was chosen for our experiments because the bandpass is narrower.

A thick lead plate was used to protect the photomultiplier against the hard x-ray directly emitted from the focus machine. The photomultiplier is contained inside a metal box which is grounded.

Using this detector, the observed soft argon x-ray is displayed in Figure 3-3-2 against the hydrogen signal. The time scale used is 200 nsec/div. The pulse width of soft x-ray is approximately 100 nsec for hydrogen and approximately 40 nsec for argon.

The second type of x-ray detector used during the latter experimental study is the PIN double diffused silicon detector. The smaller size

ENERGY (KEV)	1	2	3	4	5	6
$A_1$ (0.01cm)	.999	.945	.575	.298	.151	.095
$A_2$ (0.005cm)	.999	.807	.385	.180	.095	.052

TABLE 3-3-1 ABSORPTION FRACTION OF NE102

ENERGY (KEV)	1	2	3	4	5	6
$T_1$ ( $5 \times 10^{-4}$ cm)	.045	.600	.844	.928	.708	.803
$T_2$ ( $5 \times 10^{-3}$ cm)	.002	.368	.712	.857	.500	.644

TABLE 3-3-2 TRANSMISSION FRACTION OF TITANIUM

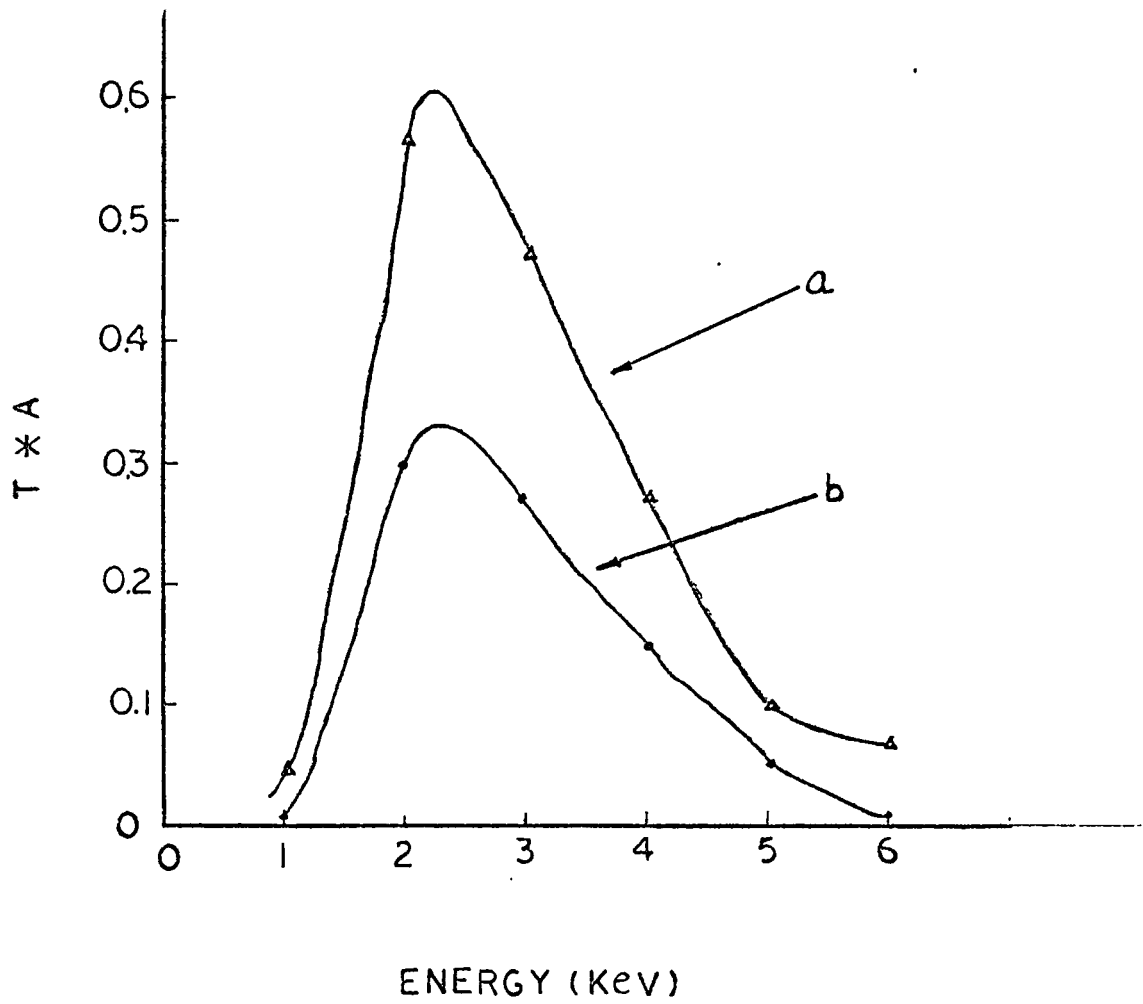


FIG 3-3-1 SENSITIVITY FOR BAND PASS FILTER

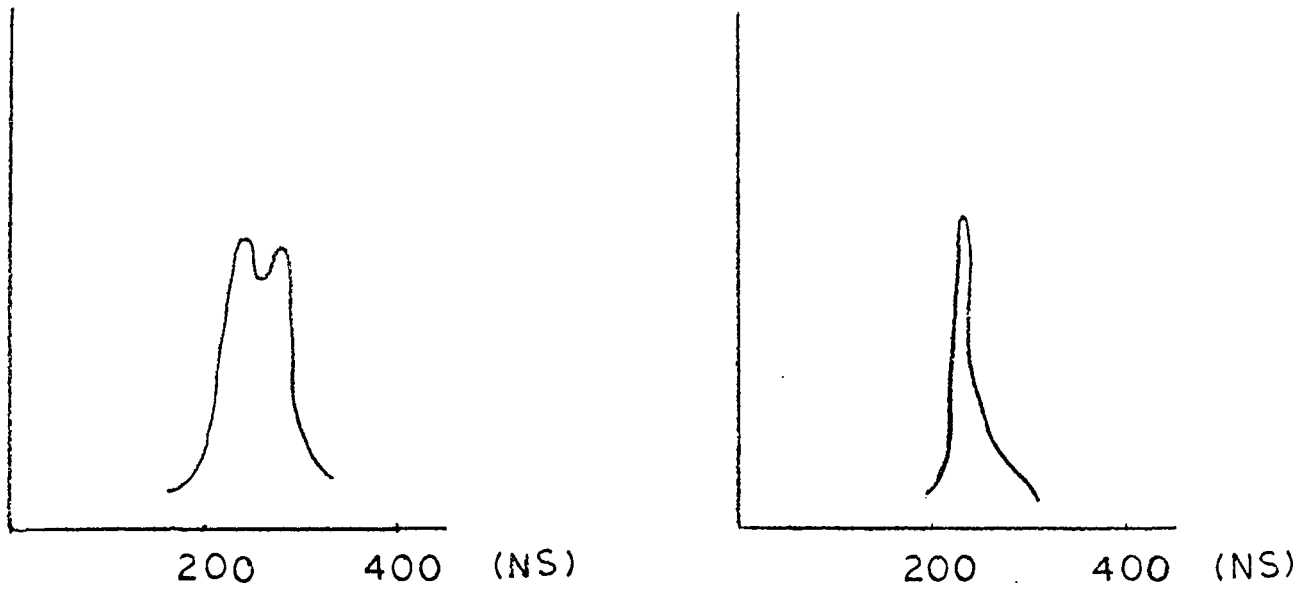


FIG 3-3-2 SOFT X RAY SIGNALS FOR HYDROGEN FOCUS(LEFT) AND ARGON FOCUS(RIGHT)

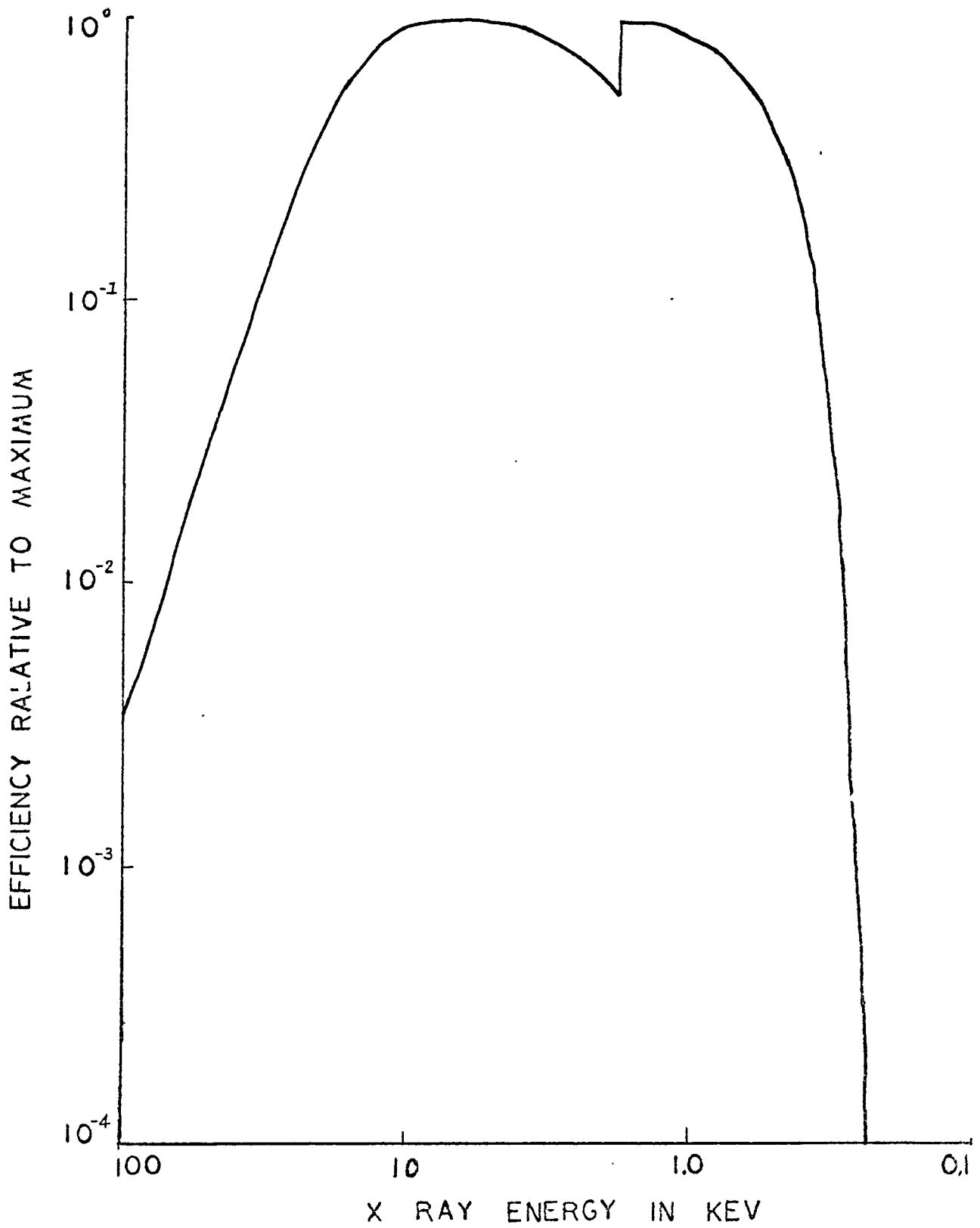


FIG 3-3-3 SENSITIVITY FOR PIN DETECTOR

of this detector allowed us to make measurements more easily. However, the narrow band energy measurement is not achievable, because of its wide range of sensitivity. Figure 3-3-3 shows the response sensitivity of this detector.

Considerable care had to be exercised to eliminate electrical pick up in x-ray detectors. A double shielding arrangement was found to be satisfactory.

A negative 300 volts bias and a load resistance of 50 ohm was used as suggested in application notes. With this arrangement a typical rise time of the signal is about 2 nsec.

#### 3-4 X-Ray Polarimeter

The x-ray polarization, has long been used to study the nature of solar flares.<sup>(20)</sup> The generation of these polarized x rays can be simply explained by the acceleration of the directed electron beams in the sun.

If we have a single electron under the acceleration  $\vec{a}$ , the electric field of the retarded radiation within the nonrelativistic domain is given by:<sup>(26)</sup>

$$\vec{E} = \frac{e}{c^2} \left[ \frac{\vec{n} \times (\vec{n} \times \vec{a})}{R} \right]_{ret} \quad (3-4-1)$$

where  $\vec{n}$  is the unit vector in the direction of observation, R is the distance between the observer and the accelerated electron. This electric field lies in the plane containing  $\vec{n}$  and  $\vec{a}$  and also is polarized in the direction perpendicular to  $\vec{n}$  (see Figure 3-4-1).

Therefore, if there is an energetic electron beam in the plasma, the collision of the electron beam with the plasma will accelerate the

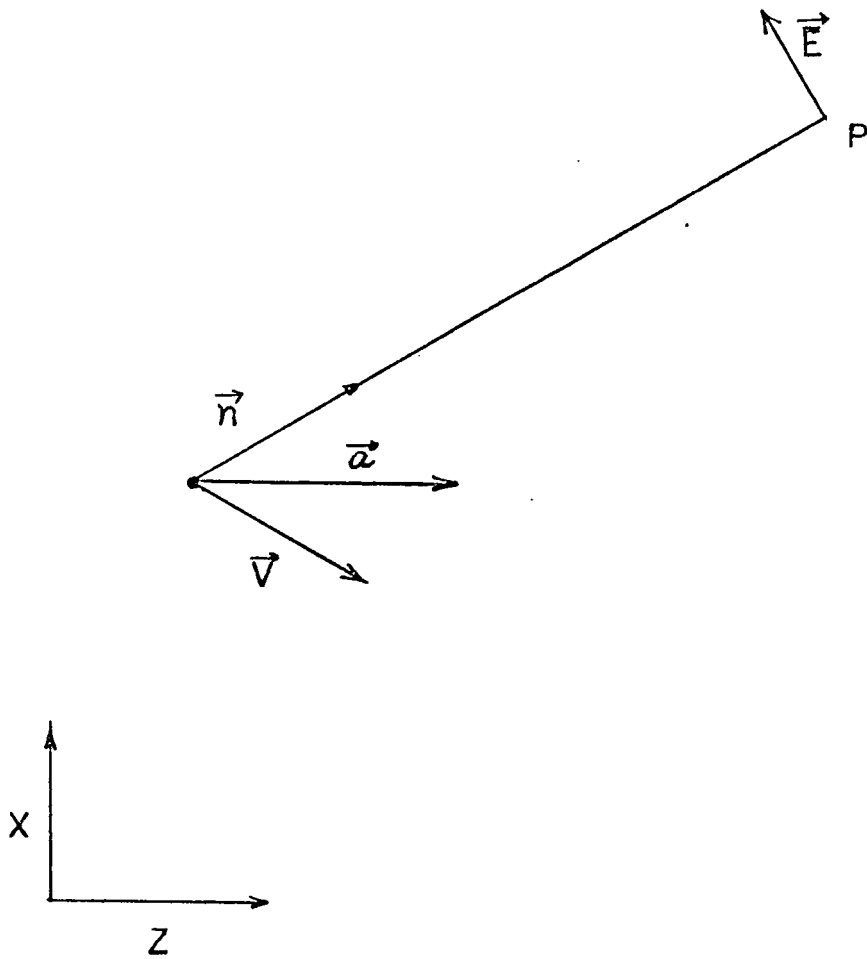


FIG 3-4-1  
ILLUSTRATION OF THE POLARIZED RADIATION FROM  
AN ACCELERATED ELECTRON

electron in the opposite direction of its velocity. The bremsstrahlung emitted from the interaction between the beam and the plasma will be polarized.

Although polarization effects are produced by the beam acceleration, it has also been shown that even with a thermal bremsstrahlung model, we might expect partial polarization of the radiation, if the velocity distribution of the source is not spherically symmetric.<sup>(21)</sup>

The design of the x-ray polarimeter is based upon the Thompson scattering theory. The azimuthal dependence of the scatter intensity from a scatterer is proportional to  $\sin^2 \theta$ , where  $\theta$  is the angle from the polarization of the incident radiation to the direction of observation. A maximum intensity will be observed at the direction perpendicular to the polarization while minimum intensity will be observed in the direction parallel to the polarization (See Figure 3-4-2).

The scattering polarimeter consists of two PIN silicon detectors mounted at the side of the scatterer. The viewing direction of the two detectors are both perpendicular to the incident beam with one detector aligned along the DPF axis while the other detector perpendicular to the axis. Figure 3-4-3 shows the aperture and the viewing directions of the two detectors. If the electrons of the plane were accelerated axially, the detector along the DPF axis will see the maximum scattering and the detector perpendicular to the axis will see the minimum scattering. If the electrons were accelerated radially the observation result will be reversed.

It has been shown both theoretically and experimentally that a complete Thompson scattering is not achievable. Considerable amount

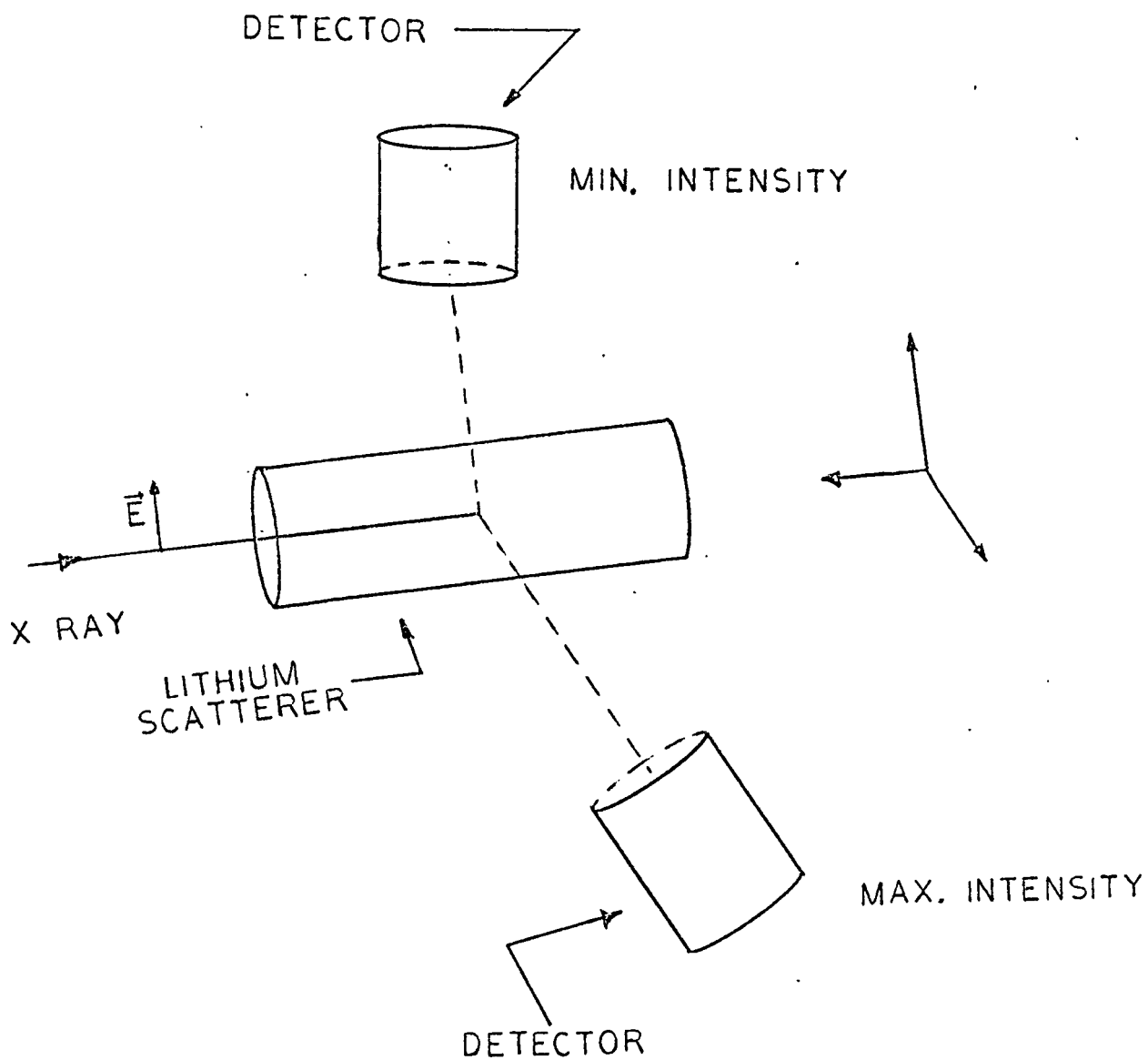


FIG 3-4-2 ILLUSTRATION OF THE ANGULAR DEPENDENCE OF THE SCATTERED INTENSITY FROM A POLARIZED X RAY BEAM

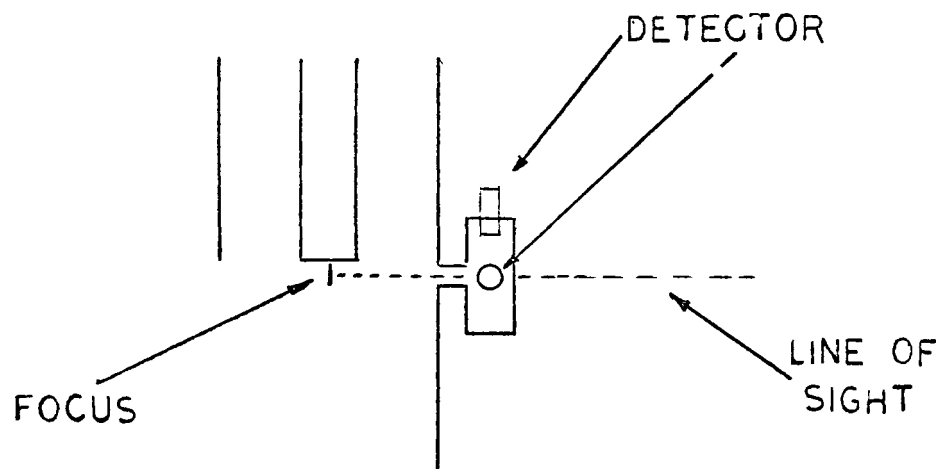
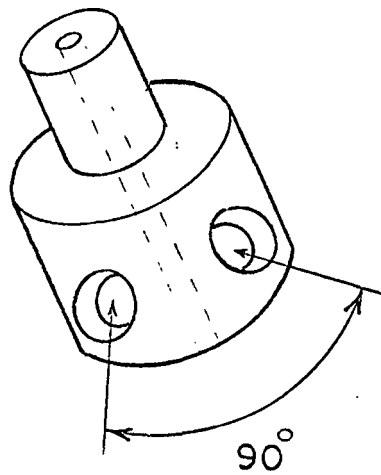


FIG 3-4-3  
X RAY POLARIMETER AND ITS VIEWING  
DIRECTION

of scattering comes from the multiple scattering, fluorescent radiation and Bragg scattering.<sup>(22)</sup> Although Bragg scattering is sensitive to polarization, the fluorescent and the multiple scattering will tend to depolarize the radiation. Therefore one must design the polarimeter to minimize the depolarization contribution.

The fluorescent radiation increases with  $Z^4$  while Thompson scattering is simply proportional to  $Z$ . The polarization scatter should be made out of material of small  $Z$  to minimize the fluorescence. A lithium block was chosen as the scatterer in our experiment. The diameter of the lithium cylinder was 0.6 cm. A size small enough so that multiple scattering effect could be neglected for the x-ray energies of interest.<sup>(21)</sup> As determined from the different absorption foils placed in front of the pinhole camera, the temperature of the thermalized plasma is about 3 keV. Therefore a length of 1.5 cm was chosen for the lithium cylinder scatterer so as to effectively scatter x-rays having energies below 6 keV.

In use, the polarimeter is pointed toward the source and rotated 90° about the line of sight between the discharges. This mode of operation avoids false indication of polarization that would otherwise arise from differences in the counter sensitivities, amplifier gains and other instrumental assymetries.

### 3-5 Crystal Spectrometer

If we can assume that the plasma velocity distribution is a Maxwellian distribution, the temperature of the plasma can be determined from the spectral characteristics of the bremsstrahlung. An x-ray

crystal spectrometer was used to obtain the relative x-ray intensity at various wavelengths and the temperature of plasma was determined from the analysis of these measurements.

A schematic configuration of the spectrometer is shown in Figure 3-5-1. The scattering crystal was mounted on a crystal plate whose orientation could be changed slightly by adjusting the screw on the back of the spectrometer. The detector was oriented to the crystal at an angle of  $44^\circ$  measured from the incident beam. This allows the detector to see the x-rays scattered by the crystals at the Bragg angle  $22^\circ$ .

Both the scattering crystal and the x-ray detector were assembled inside a 2" diameter aluminum tubing so that helium can be filled into the spectrometer for soft x-ray measurement.

The crystals used in the spectrometer are LiF (220), Si (220), and Graphite (002), which can scatter the x-ray wavelengths respectively at  $1.07\text{\AA}$ ,  $1.44\text{\AA}$ , and  $2.5\text{\AA}$ , into the x-ray detector.

Due to the shot to shot variation of the focus x-ray emission, the ratio of the intensity of the x-rays scattered at a given wavelength to the total x-ray source intensity was measured. The ratio was obtained by using two PIN detectors simultaneously. One of the detectors was used to observe the scattered x-rays from the crystal while the other was used to measure the radiation coming directly from the plasma focus. The relative intensity of the specified wave length was obtained by calculating the ratio of these two signals.

A window for observing the x-ray source was 0.4 cm in diameter and was vacuum sealed by 0.002" Mylar. A 0.0005" Be foil was placed behind the Mylar to shield out the visible light. The spectrometer

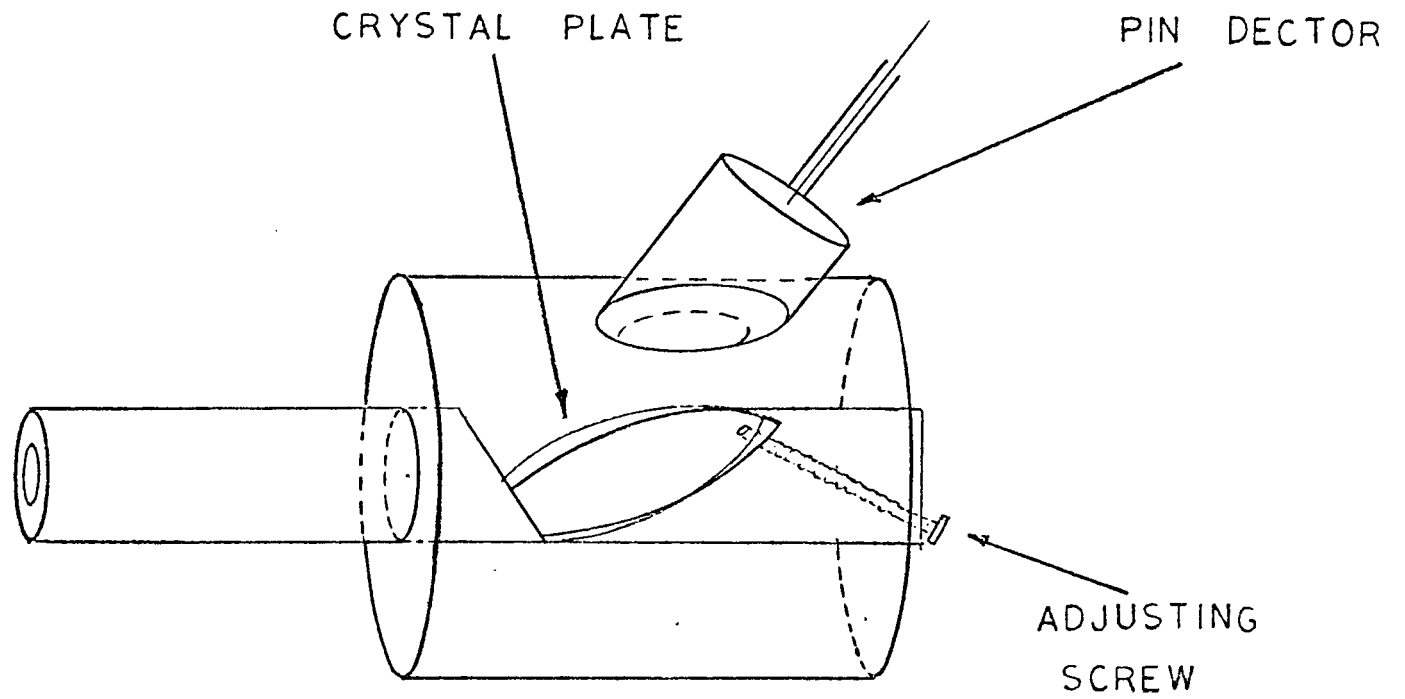


FIG 3 - 5

X RAY SPECTROMETER

viewed the focus at an angle of  $68^\circ$  measured from DPF axis and at a distance of approximately 26 cm from the plasma focus.

## CHAPTER 4

### DISCUSSION OF EXPERIMENTAL RESULTS

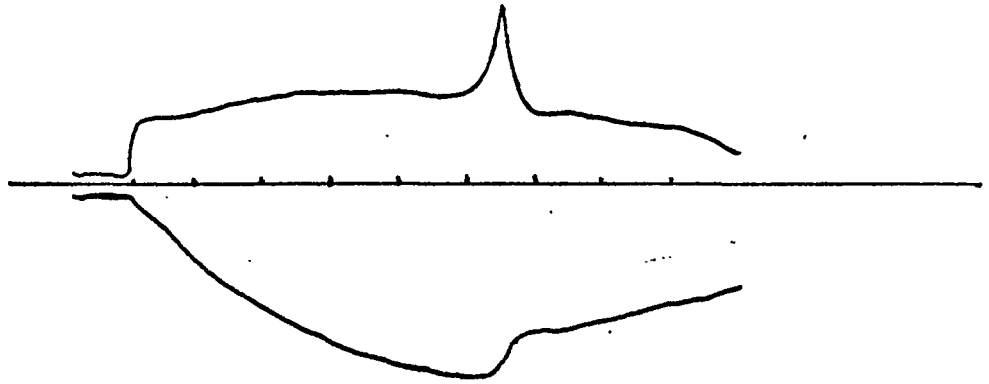
#### 4-0 Introduction

In this chapter we will describe the experiments which we have done on the DPF discharge in argon. Data will be presented and the results will be analyzed.

In the first section we will describe some general macroscopic phenomenon to explain the observed voltage and current traces, such as the speed of current sheath, the thickness of the shock wave and the applicability of the snow plow model. Next, a series of x-ray studies will be described and analyzed. These experiments are the spatial and temporal studies described in Section 2, correlation of the x-ray and voltage signals described in Section 3, polarization of x-rays described in Section 4 and the spectrum determination described in Section 5.

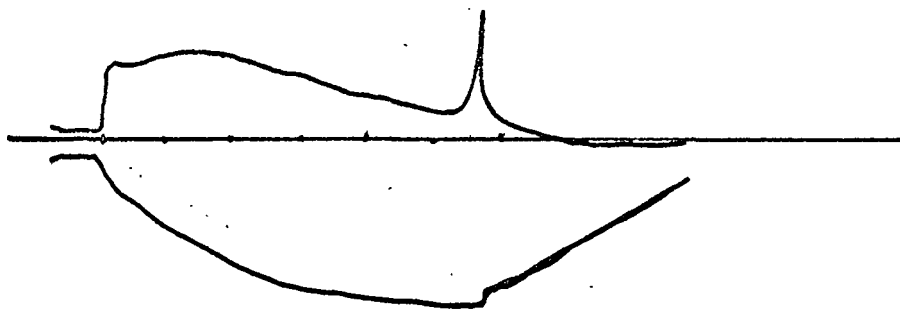
#### 4-1 Voltage and Current Measurement

Figure 4-1-1 shows the voltage and current traces obtained for the DPF operating with argon and with hydrogen. Comparing the voltage traces obtained from these two different gases we can see the following differences: (1) The voltage in the argon discharge shows a gradual decrease during the run-down phase, while that for the hydrogen discharge



500 NSEC/DIV

VOLTAGE AND CURRENT TRACE  
IN HYDROGEN



500 NSEC/DIV

VOLTAGE AND CURRENT TRACE  
IN ARGON

FIG 4-1-1

remains more or less a constant. (2) The voltage spike which appears at the final collapse is much narrower for argon than for hydrogen.

The first difference was expected. Based on the snowplow model, the traveling velocity of the current sheath is inversely proportional to  $\rho_0^{1/4}$  where  $\rho_0$  is the initial gas density. The greater mass of the argon atom, as compared with that of hydrogen atom, implies that the argon current sheath travels at a slower speed than the hydrogen current sheath. This slower current sheath speed results in a slower variation of the circuit inductance, and the induced voltage will not be able to cancel the decrease of the applied voltage. On the other hand, the hydrogen current sheath is traveling fast enough to generate an induced voltage which is sufficiently large to sustain the voltage despite the decrease of the applied voltage.

Based on the time measured from the initial breakdown to the final collapse and the length of the electrode, the hydrogen current sheath travels at an average speed of approximately  $8 \text{ cm}/\mu\text{sec}$ ; while the argon current sheath travels at an average speed of approximately  $3.3 \text{ cm}/\mu\text{sec}$ .

The second phenomenon observed was not in accord with our expectations of a slower collapse for argon, based on invoking a simple snowplow model in order to explain the final pinch. This snowplow model predicts that the argon spike width should be about three times longer than that for hydrogen. However, the duration of the observed argon voltage spike is approximately 80 nsec while that for Hydrogen lasts approximately 200 nsec.

The reason for this discrepancy can be understood by comparing the



X RAY PINHOLE PICTURE OF H<sub>2</sub> DPF



X RAY PINHOLE PICTURE OF ARGON DPF

FIG 4-1-2

time integrated pinhole pictures for these two different gas discharges. Figure 4-1-2 shows the integrated pinhole pictures for hydrogen and argon. We see that hydrogen focus length is much longer than that for argon. If we compare the x-ray pinhole focus length with the duration of voltage spike, we find that the hydrogen focus column is not formed simultaneously on the axis at all points and thus has a longer duration.

Comparing the current traces of the two discharges, we can see that at the time of collapse the current drops considerably for the hydrogen discharge, but hardly at all for the argon discharge. We believe that this phenomenon can be explained relatively simply by examining the different nature of shocks in the two gases. The argon shock wave was previously shown to be thicker than that of hydrogen. This increase in shock thickness causes a smaller electric field during the argon focus formation. The induced electric field is thought to cause the current decrease, and since the induced electric field is smaller for argon, the amount of current decrease is also correspondingly smaller.

#### 4-2 Spatial and Temporal Studies

Time integrated x-ray three pinhole pictures have been used to study the spatial variation of the plasma focus. The principle of the pinhole camera in the x-ray region of the spectrum is essentially the same as that of a standard pinhole camera. The object and the image will be inverted relative to the pinhole axis as shown in Figure 4-2-1.

The pinhole camera has been used quite extensively to photograph plasma by x-ray radiation. Here we use three pinholes, each covered with different absorber foil, in order to obtain three simultaneous but

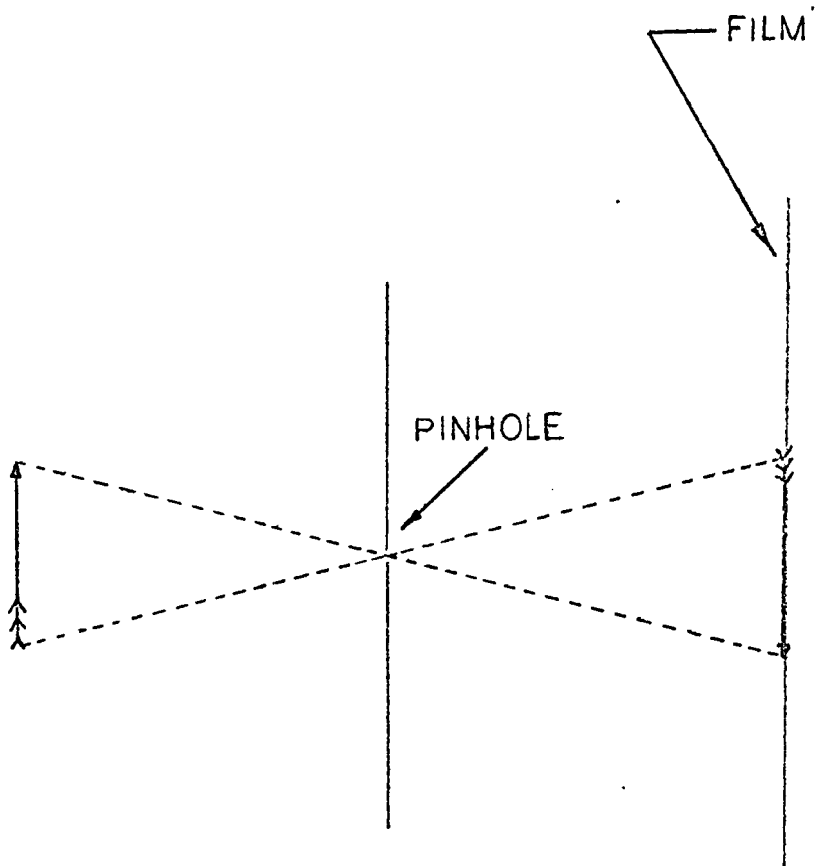


FIG 4-2-1  
ILLUSTRATION OF THE PRINCIPLE FOR A PINHOLE CAMERA

different spectral views on the plasma focus.

The size of the pinholes of our experiment is 0.25 mm in diameter. Pinhole pictures were taken from two different directions,  $75^\circ$  and  $0^\circ$  measured with respect to the DPF axis, to aid in obtaining a three dimensional representation of the plasma focus.

Both type 47 and type 57 polaroid films were used. Type 47 film is sensitive to x-rays of energy less than 5 keV while type 57 film is specifically designed to respond to x-rays with energy up to 30 keV. A thin piece of black paper was used over the type 57 film to eliminate the x-rays having energy below 5 keV. Therefore, picture obtained with type 57 film shows only the regions emitting hard x-rays.

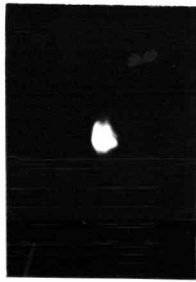
It is necessary to fill the region between the foil covered pinhole and the film with helium if one wishes to photograph x-rays softer than a few keV. Without the helium, the argon plasma focus can hardly be seen on the soft x-ray picture. In the soft x-ray camera, the distance from the pinhole to the film plane was 12 cm. The distance from the region of the plasma focus to the pinhole was 40 cm when the camera was viewing at  $0^\circ$ , and 15 cm when the camera was viewing at  $75^\circ$ . No helium was required when the hard x-rays picture was photographed. For the hard x-ray camera, the distance from the pinhole to the film plane was 30 cm at  $0^\circ$  and about 10 cm at  $75^\circ$ . The distances from the pinhole to the plasma focus were the same as those for the soft x-ray camera. Figure 4-2-2 shows the pinhole pictures obtained for both soft and hard x-rays at the two directions. The foils used at the three pinholes were  $0.001''\text{Be}$ ,  $0.005''\text{Ti}$  and  $0.002''\text{Cu}$ . It should be noted that these pictures are time exposures and indicate the time

integrated structure of the focus. Figure 4-2-2-a shows the soft x-ray pinhole camera photographs with viewing angle at  $75^\circ$ . The foils covering the pinholes on the right side image is 0.002 Cu., the middle one is 0.005 Ti and the left is 0.001 Be. As the absorption coefficient decreased, the halo of the electrode image showed more and more clearly. The most intense emission is from the portion which is nearer the surface of the electrode. This is because a higher plasma density was generated in the vicinity of the electrode surface. This higher plasma density is characterized by the lower electron energy caused by heat conduction of the electrons and the pressure balance along the current sheath.

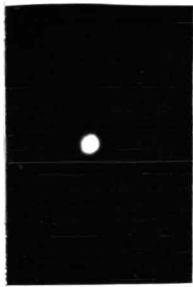
Figure 4-2-2-b shows the soft x-ray photographs with viewing angle at  $0^\circ$ . The foil arrangements are the same as in Figure 4-2-2-a. The decrease of the image diameter with increased foil absorption indicates that both the density and/or temperature of the plasma decrease with increasing radius. The circular shape of the image indicates the collapse is symmetric.

Figure 4-2-2-c shows the hard x-ray photographs at  $75^\circ$ . The foil arrangements are the same as Figure 4-2-2-a. No hard x-ray photons were seen to originate from the plasma column region. The intense emission from the electrode surface indicates the existence of high energy electrons. The lack of symmetry seen in the central bright region is typical for the hard x-ray pinhole pictures; its origin is not understood.

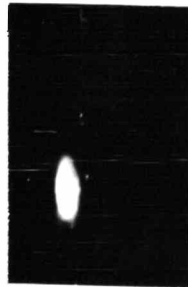
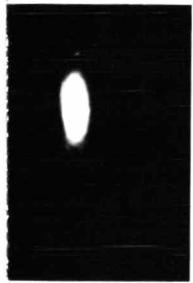
Figure 4-2-2-d shows a hard x-ray single pinhole photograph viewed at  $0^\circ$  position. The purpose of using a single pinhole instead of three



(a)



(b)



(c)



(d)

FIG 4-2-2 SOFT AND HARD X RAY  
PINHOLE PICTURE OF ARGON DPF

pinholes is because its alignment is much easier. The brightest spot surrounded by the less intense halo is typical for all of the pinhole pictures. Vortices can be observed in the halo region with this hard x-ray camera position.

Comparing the argon soft x-ray photograph with that typically obtained for hydrogen, we see that the length of the argon focus is only about 1/5 of that obtained in hydrogen, while the column diameter appears to be about the same for the two cases. This difference in length is possibly caused by the slower velocity of the sheath as it arrives at the end of the electrode during the run down state.

Comparisons between the soft and hard x-ray pictures for the argon focus indicates that the soft x-rays originate from thermal bremsstrahlung emitted from the dense plasma column while the hard x-rays are generated by the nonthermal energetic electrons bombarding the electrode surface or thick target bremsstrahlung. These high energy electrons have a small collision frequency in the thermal plasma, so that the principal region for hard x-ray emission is the surface of the electrode and the plasma column will not be imaged in the hard x-ray picture.

Although an x-ray pinhole camera pictures gives useful information on the spatial distribution of the sources, it does not give any information on the temporal development. To study the temporal variation of the x-ray radiation, the plasma was viewed with fast solid state x-ray detectors. Two PIN detectors were used to observe the focus through 4 mm diameter apertures. A variety of foils were used to obtain information on the spectral properties. These foils were 0.005"Ti, 0.002" Cu., and a combination of 0.0006" Au with 0.002" Cu. Two

detectors with different absorption foils were used simultaneously to give a time comparison of different spectrum regions and also to eliminate probable error arising from shot to shot variations. Typical results obtained with different foils are shown in Figure 4-2-3.

All these signals show a big spike having a rise time of about 15 nsec and a half width of about 40 nsec. However, different foils showed different time of signal decay after the big spike, indicating that the temperature of the plasma was gradually decreasing in the time following the spike.

The intensity of the bremsstrahlung radiation emitted per unit frequency from the Maxwellian plasma at temperature  $T$  is:<sup>(24)</sup>

$$I_{\lambda} = A \frac{n_i n_e Z^2}{\lambda^2 (kT)^{1/2}} e^{-h\nu/kT} \quad (4-2-1)$$

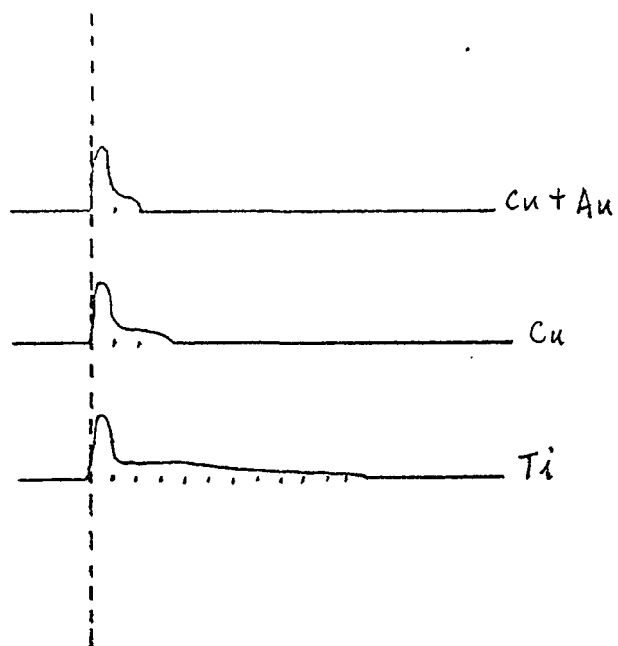
where  $h\nu$  represents the energy of the photon.  $\lambda$  is the corresponding wave-length,  $n_i$  and  $n_e$  are the ion and electron densities respectively,  $Z$  is the nuclear charge, and  $A$  is a constant depending on the unit chosen.

From the above equation we can say that the intensity of radiation depends much more strongly on the plasma density than temperature. Furthermore, if we assume that the plasma is compressed adiabatically the temperature and density are related by the equation:

$$\frac{T}{\gamma^{r-1}} = \text{const.} \quad (4-2-2)$$

where  $\gamma$  is the ratio of the specific heat and is between 1.67 and 1.48 for ionized argon.<sup>(25)</sup>

Equation (4-2-2) indicates to us that the temperature and the density



40 NSEC/DIV

X RAY SIGNALS WITH DIFFERENT  
ABSORPTION FOILS

FIG 4-2-3

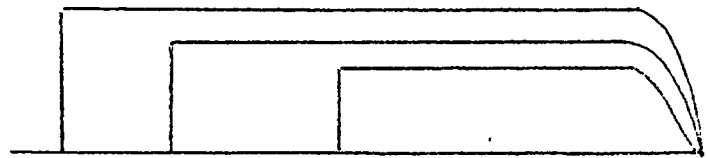
are related and rules out the possibility that one variable changes more drastically than the other. Since the intensity of the bremsstrahlung radiation is dominated by the density of the plasma, we can conclude that the time of occurrence of the initial spike of the x-ray signals corresponds to the time when the density of the focus is maximum.

The differences between the signals seen with various filters allows us to draw some conclusions about the later stage of the focus, after maximum density.

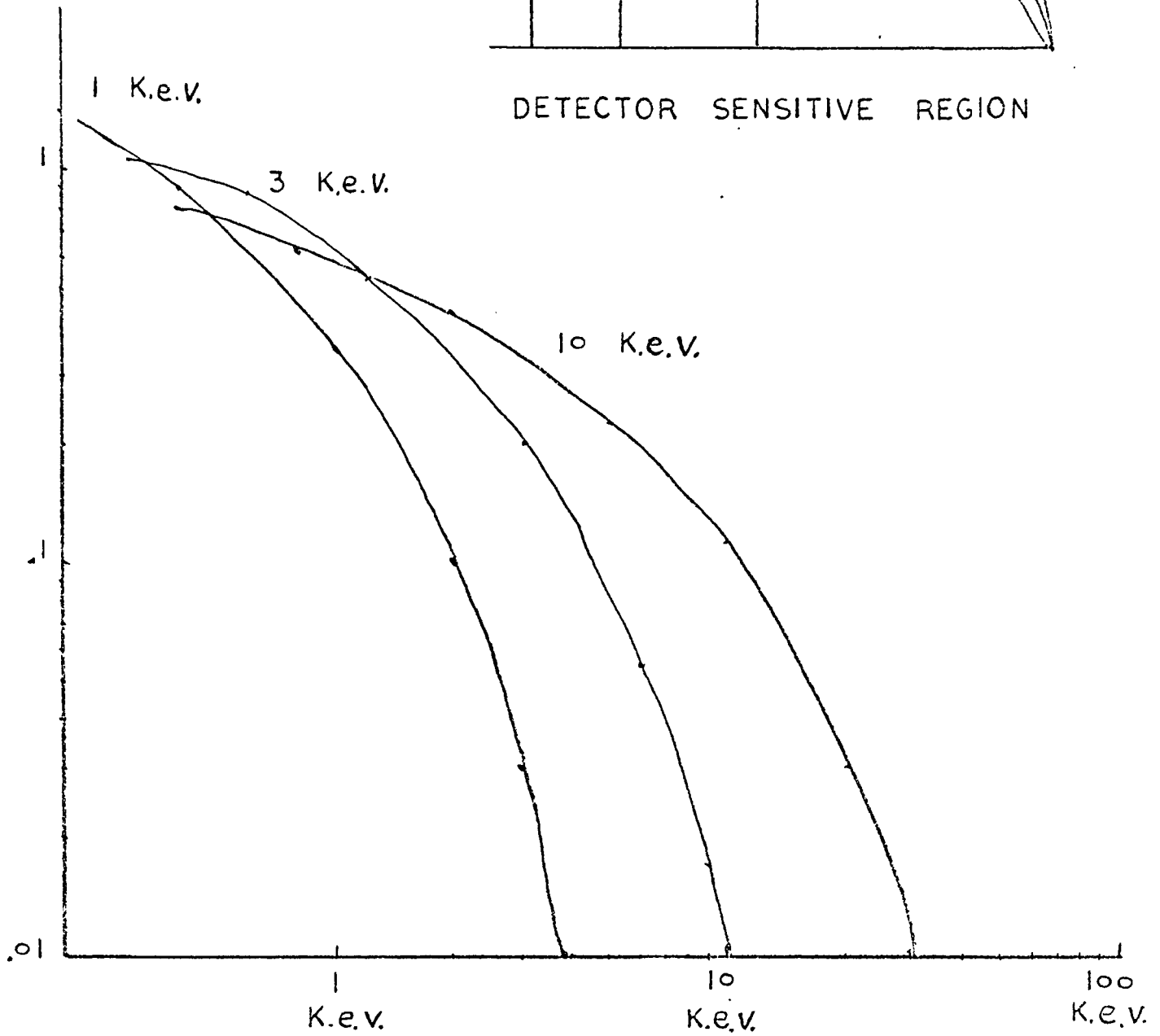
Based on equation (4-2-1), if the temperature of the plasma were constant and the density of the plasma were decreasing, the shape of the over all bremsstrahlung spectrum would not be changed, but the intensity would decrease due to the density decrease. Since our detector responds linearly, we can not associate the different decay times for different energy channels with the decreasing density. The decay of the plasma takes place over a time of about 100 nsec. It is reasonable to assume that the plasma is thermalized and not strongly turbulent.

Figure 4-2-4 shows the bremsstrahlung spectrum of a thermalized plasma calculated from equation (4-2-1) at temperatures of 10 keV, 3 keV and 1 keV. As the temperature of the plasma decreases the spectrum of the emission shifts to the softer photon region. In the same figure the sensitive regions of the detector coupled with different absorption foils are also shown.

As the plasma temperature decays, the bremsstrahlung spectrum shifts toward the softer region and moves out of the sensitivity area of a specified detector. Therefore, from the analysis of the fading points of the signals on Figure 4-2-3 and the lower limit of the detector's



DETECTOR SENSITIVE REGION



THERMAL PLASMA BREMSSTRAHLUNG

FIG 4-2-4

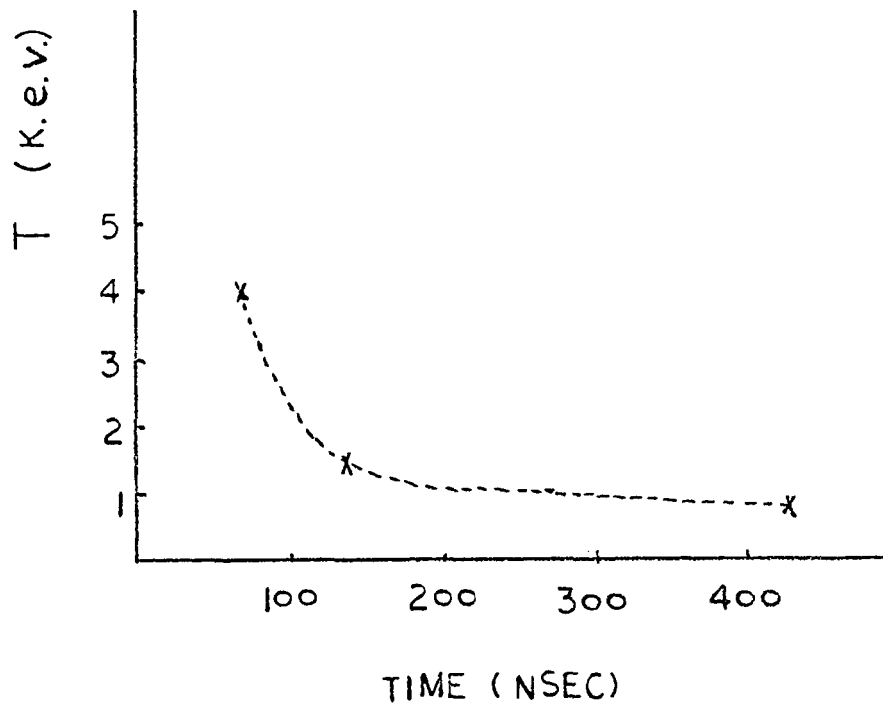
sensitivity. We can infer the temperature dependence of the plasma after its maximum compression. The profile of the decreasing temperature is shown in Figure 4-2-5. The data points were obtained by setting the lower limit of the sensitivity of the detector to the 1% of the bremsstrahlung spectrum function.

The temperature of the plasma appears to decay exponentially with time, however, if we plot the three data points observed using a similogarithm plot they do not lie on a straight line. Therefore, some other temperature decay characteristic must be considered. It was surprising to find that the three data points lay on a straight line when  $1/T^3$  was plotted against time. This behaviour is exactly the same as that exhibited by a body cooling by black body radiation.

We must, however, rule out the possibility that the focus is cooling like a black body, since it is not opaque to its emitted x-ray radiation. Since the detectors were observing radiation from both the electrode and the plasma, we conclude that the observed time variation of the output is associated with the surface radiation and may not really be thermal in character.

It should be noted that when using the fastest sweeps of the oscilloscope, the spike feature often shows some structure, however, this feature is not very reproducible.

Although the pinhole camera shows the hard and soft x-rays originates from different regions, it tells us nothing about the relative times of occurrence of these features. Unfortunately the detectors measuring the time variation have no spatial resolution. To achieve a better



TEMPERATURE DECAY OF DPF

FIG 4-2-5

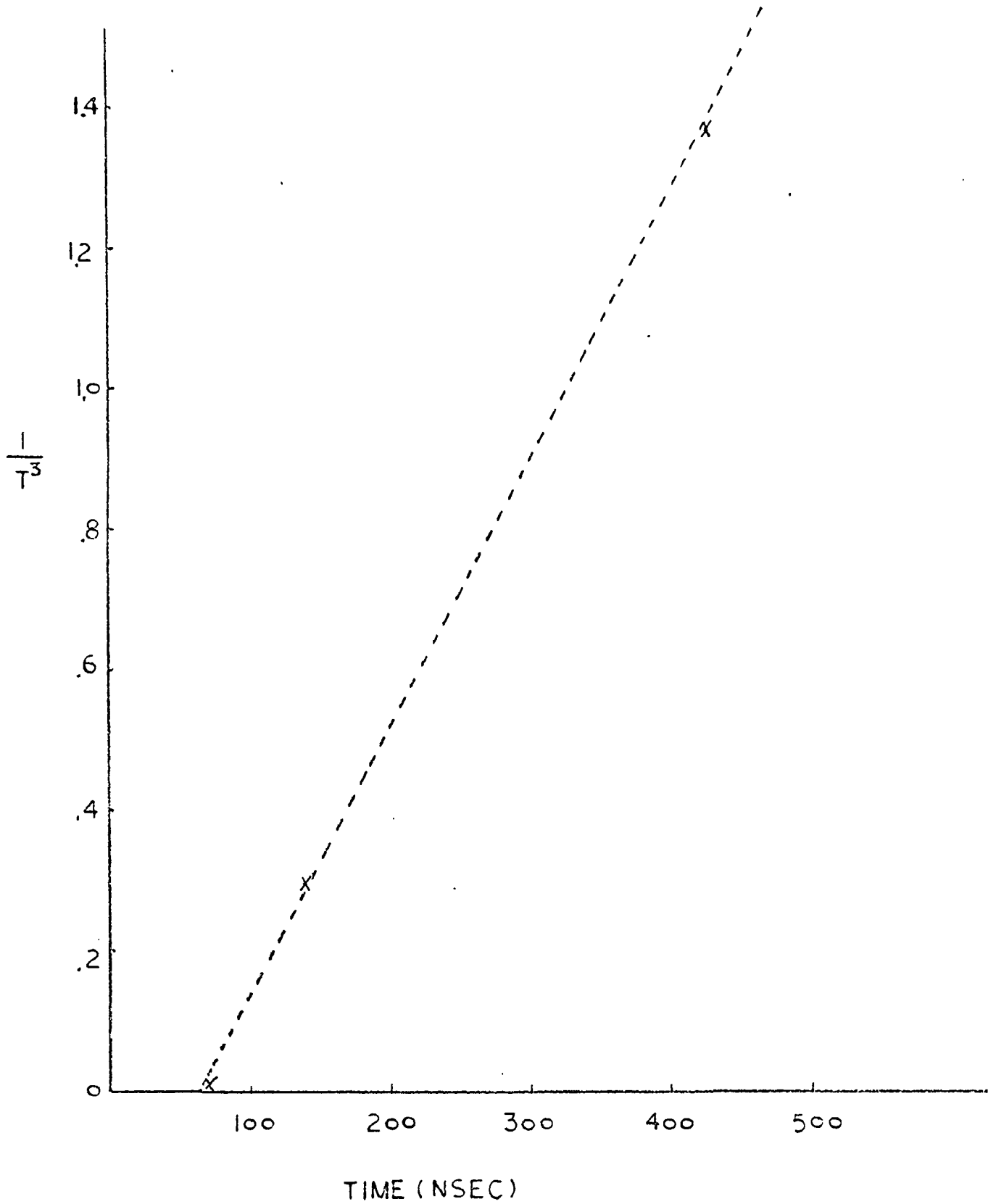
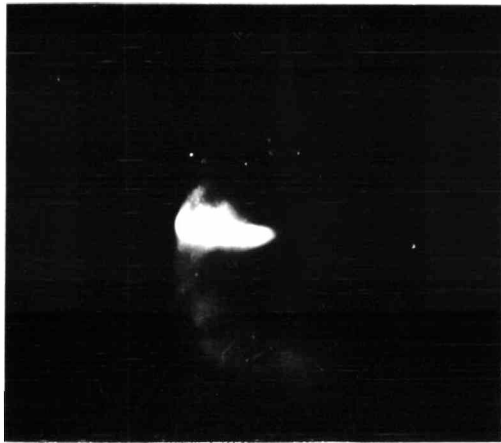


FIG 4-2-6 TEMPERATURE DECAY OF DPF

understanding, the resolution in time of x-rays emitted from different points along the column and different radial positions on the electrode surface is necessary.

The technique employed a pinhole to form an enlarged image of sufficient size so that the PIN detectors could be placed to receive the radiation from a distant region. To allow the two detectors to be placed side by side so that the comparisons could be made between regions, the magnification required is about five. A 27" long 3" diameter tubing was attached behind a pinhole covered with a Be foil 0.001" thick. Type 47 and 57 films were used to obtain soft and hard x-ray pictures. Figure (4-2-7) shows both the soft and hard x-ray magnified pinhole pictures taken at the end of this 27" tubing. It was necessary to fill the camera tube with helium to obtain the soft x-ray picture. The magnified soft x-ray pictures shows quite clearly the  $m = 0$  mode M.H.D. wave which develops on the surface of the column. The fastest growing mode has a wave-length of 0.6 mm. The crossed dark line shown on the magnified hard x-ray picture is the image of the copper strips used for alignment purposes. Figure (4-2-8) shows another set of magnified x-ray pinhole pictures taken behind the flange used for holding the detectors in place.

Since the time different of the peak x-ray emission from various points of the focus was expected to be small, it was important to use a broad band oscilloscope and as rapid a sweep as possible to display these signals. In order to measure any difference in times of emission from different regions, the Textronik type 454 oscilloscope was used. However, this oscilloscope has only a single beam, therefore, it was



SOFT X. RAY PICTURE

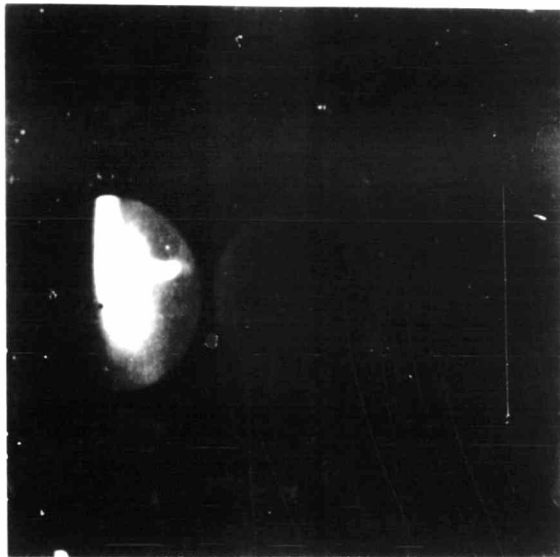


HARD X RAY PICTURE

FIG 4-2-7 MAGNIFIED SOFT AND HARD  
X RAY PIN HOLE PICTURES OF ARGON  
FOCUS



SOFT X RAY PICTURE



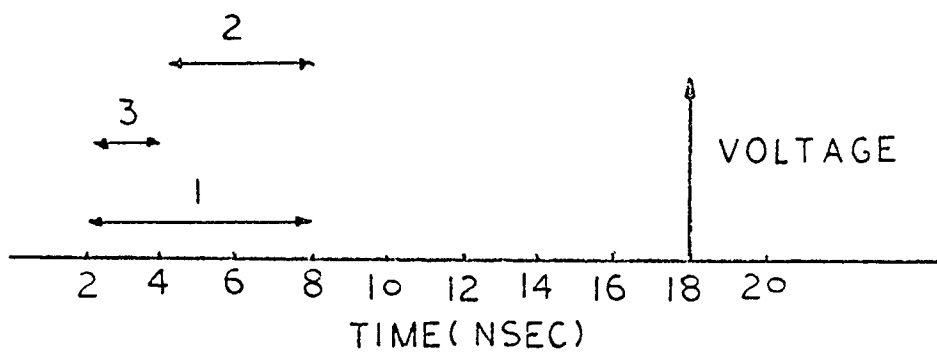
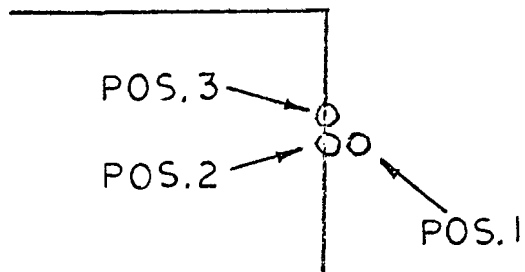
HARD X RAY PICTURE

FIG 4-2-8 MAGNIFIED SOFT AND HARD  
X RAY PICTURES OF DPF VIEWING BEHIND  
THE DETECTOR HOLDER

necessary to arrange a scheme for displaying two signals on this single sweep of the scope. The voltage spike produced in the collapse was used to trigger the oscilloscope sweep and was also displayed on the oscilloscope after going through a 120 meter coaxial cable which produced a 420 nsec delay. The detector output for the x-ray signal was fed into the scope directly without additional delay. Use of the "add" mode of the input amplifier allowed the two signals to be mixed with proper impedance matching and to be displayed at different positions on the trace.

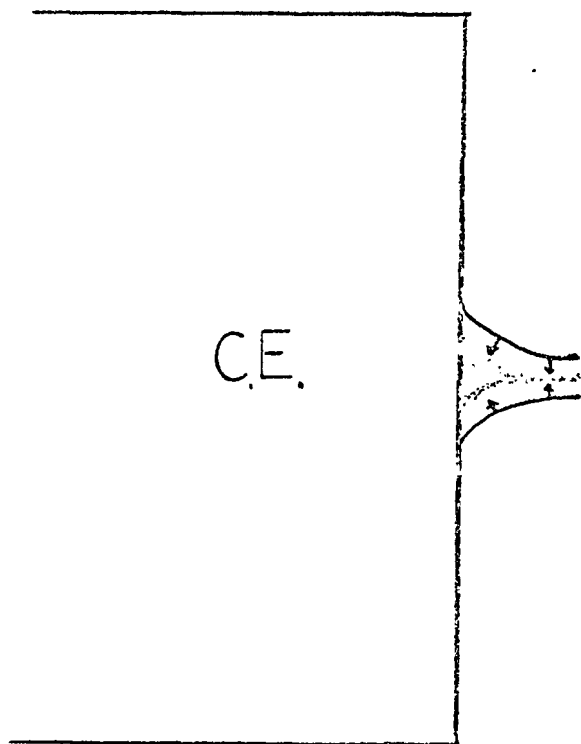
The time difference between the x-ray peak and the voltage peak shown on the polaroid film were measured. After subtracting 420 nsec, which was caused by the delay of the 120 meter cable, the results for space and time resolved measurement are obtained and displayed in Figure 4-2-9. The results obtained from several discharges are used to define a region of time over which the occurrence of the x-ray peak is most probably expected to occur. The labels used are as follows: position 1 is at the tip of the focus column, position 2 is at the center of the electrode surface and position 3 is at a point located a few millimeters above the center of the electrode surface.

The time of occurrence of the peak of the x-ray signals falls within 6 nsec of each other regardless of the source location, however, the emission from position 2 appears to be a few nsec later than that emitted from either position 1 or position 3. Based on this observation we therefore propose the following model for the behaviour of the plasma sheath over a time interval just before and up to the final collapse. The temperature near and adjacent to the inner electrode is reduced by



OCCURRENCE OF X RAY PEAK  
EMITTED FROM DIFFERENT REGIONS

FIG 4-2-9



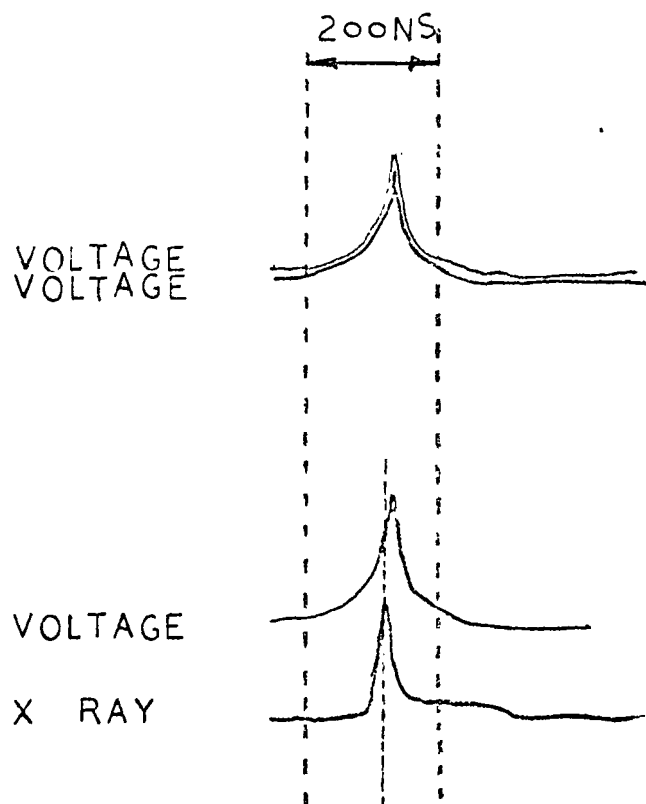
SHAPE OF CURRENT SHEATH  
BEFORE PLASMA FOCUS IS FORMED

FIG 4-2-10

electron heat conduction. Hence, to obtain the pressure balance along the shock, the plasma density adjacent to the wall rises. These high density regions will move at a slower speed than the regions at a distance from the electrode surface. Therefore, a bell shape current sheath is formed with the base toward the electrode as shown in Figure 4-2-10. The current sheath at a distance from the electrode surface can move radially, however, the sheath at the position closer to the electrode surface moves both radially and axially inward. Therefore, the tip of the focus column can be formed at the same time the current sheath along the electrode surface reaches position 3. Since the curvature of the current sheath is different from shot to shot, the time of occurrence of the peak intensity at these two positions is also going to be slightly changed. After these two points were reached, the current sheath continues to contract and reaches the electrode center about 3 nsec later.

#### 4-3 Correlation Between the Voltage and X-Ray Signals

One of the most interesting features of this work was found in connection with the study of the time development of x-ray signals of different spatial regions. Although slight differences were found for the occurrence of peak x-ray signals at different points, all points showed peaks at times well before the occurrence of the voltage spike characteristics of focus formation. Figure 4-3-1 shows examples of both voltage and x-ray signals displayed on different traces on the Tektronik 551 dual beam oscilloscope. In order to ascertain if there were differences in the two sweeps, the same voltage signal was displayed



VOLTAGE AND X-RAY CORRELATION

FIG 4-3-1

on both traces. No difference of consequence can be seen in Figure 4-3-1. The cables carrying the x-ray and voltage signal were adjusted to be within 30 cm of each other in length so that the cable induced delay is under 2 nsec. The observed time difference between the time of occurrence of the voltage and the x-ray peaks respectively is of the order 20 nsec.

The x-ray signals rise in about 15 nsec to a peak value and falls in 25 nsec to some residual value. Considering the fact that the x-ray intensity is most sensitive to the density, we can estimate that the dense plasma lasts about 40 nsec. At this time the voltage signal has reached a maximum value while the x-ray signal has fallen to the residual value and starts to decay. Based on these observed voltage and x-ray signals we now propose a dynamical model of the focus development along the following line.

The voltage peak occurs at some 20 nanosecond after the time of peak density, with which the peak x-ray signal is associated. The voltage measured in our experiment contains the ohmic component and the inductive component. At the beginning of the focus formation, the particles are rapidly pinched to a small column. The induced voltage of the current sheath collapse will cause the voltage to rise, while the rapid increase of the plasma density will enhance the x-ray emission.

When the focus reached its maximum density at the time of the peak x-ray emission, the radius of the plasma column reaches its maximum value. At this point the magnetic pressure is balanced by the dynamic pressure of the plasma. However, the column is only quasi stable and the  $m=0$  mode MHD wave develops rapidly from fluctuations on the surface

of the plasma column. Based on the theory of Spitzer the growth rate of the  $m = 0$  instability of the measured wave-length ( $\lambda \sim 0.6 \text{ cm}$ ) is within a one or two nanoseconds.

At this time the plasma current is largely on the surface of the focus column. However, the resistivity of the column at the surface could be comparatively high. The strong magnetic field then diffuses rapidly into the focus column, and the plasma will start to expand and diffuse into the magnetic piston. Holographic pictures taken on Hydrogen focus show there is a strong axial flow of particles and much of the plasma will be removed by the "axial jet". The density of the plasma will start to decrease. The rapidly changing magnetic field induces a strong electric field which tends to accelerate the plasma electrons in the opposite direction of the applied field. The drift velocity between the electrons and ions will gradually increase in the presence of this induced electric field. As is well known, if  $V_d / V_{the} \geq (m_e / m_i)^{1/2}$ , the ion acoustic instability can develop. Here  $V_d$  is the electron-ion drift velocity,  $V_{the}$  is the electron thermal velocity  $m_e$  and  $m_i$  are the electron and ion masses respectively. For the argon plasma, this condition is relatively easy to satisfy. The development of the ion-acoustic instability leads to an increase in the resistivity of the plasma, and thus anomalous resistance will lead to an increase in voltage across the focus provided that current remains constant.

If we assume the onset of the ion-acoustic instability occurred at a couple of nanosecond after the maximum compression, and that the voltage signal rises over a period of time comparable to the growth rate of the ion-acoustic instability, the time delay between the voltage and

x-ray peaks should be of the order of the growth rate of the ion-acoustic instability.

If one uses an approximate formula for this growth rate  $\omega_{pi} (m_e/m_i)^{1/2}$  and assumes that plasma density at this time is of the order of  $10^{18}$ , the calculated growth rate of the ion-acoustic instability is of the order of  $2 \times 10^8 \text{ sec}^{-1}$  and is indeed comparable to the time delay between the x-ray and voltage peak (20 nsec).

As a result of the increase in resistivity, the temperature of the plasma increases by the ohmic heating process. The resistance of the plasma calculated from ohm's law is about 0.05 Ohm. The energy absorbed during the heating process is  $RI^2 \Delta t \approx 250 \text{ Joules}$ , sufficient to heat the  $10^{16}$  particles contained in the focus region up to a temperature of 10 keV.

The ion-acoustic wave is ultimately limited by the slowing down of the drift velocity due to collisions and after the temperature of the plasma has been raised, the resistivity will go down and the voltage signal will decrease.

#### 4-4 Angular Distribution and Polarization of the X-Ray Emission

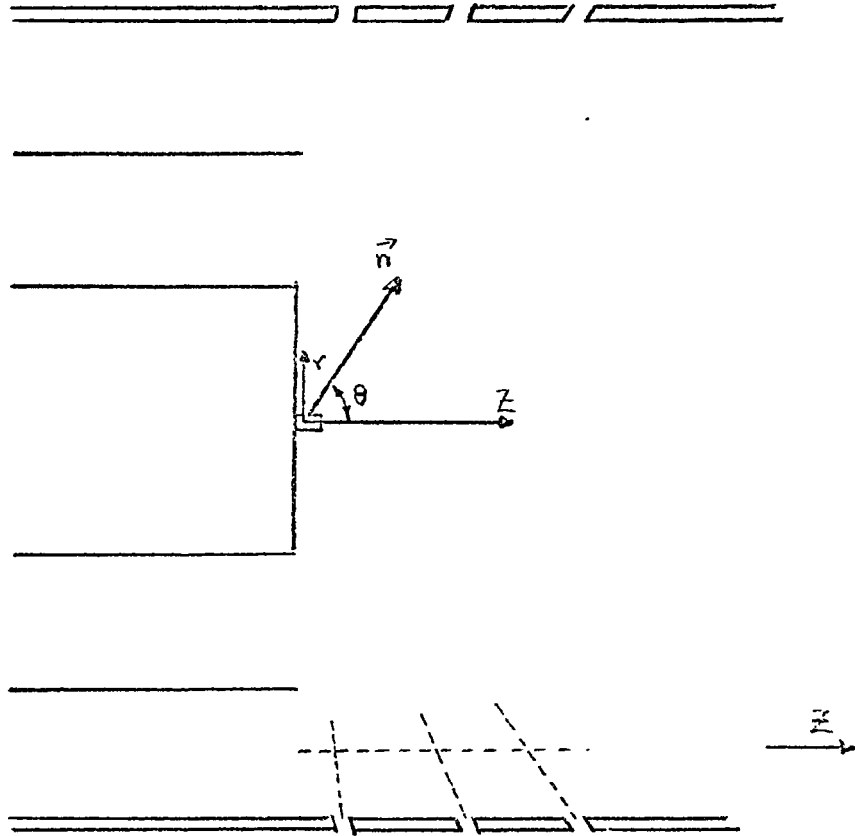
The angular distribution of the DPF peak radiation in the x-ray domain has been studied by using two PIN detectors, viewing at two different directions simultaneously. The viewing windows are made of 4 mm holes covered by 0.001Be foil located at four different directions which are at angles of  $0^\circ$ ,  $53^\circ$ ,  $68^\circ$ , and  $83^\circ$  measured from the DPF axis. A line passing normally through the center of each hole would intersect the electrode center with an uncertainty less than  $2^\circ$ . One of the PIN

detectors was used as a reference and was used to observe the x-ray emission at  $0^\circ$  for all the discharge, while the other detector was moved to the different angular position to obtain the angular distribution. The ratio of the peak intensity at the same angle to that observed at  $0^\circ$  is the observation data on which the analysis is based.

In order to eliminate differences in the detector, initial calibration runs were made in which the two detectors were placed side by side and their output signals were compared. The gains on each trace of the Textronix 551 oscilloscope were adjusted so that the signal output of each detector was the same. The same gain settings were maintained in the subsequent measurements. A minimum of 10 shots were observed for a given direction in order to obtain a suitable average relative intensity. The angular distribution intensity was measured independently in two azimuthal directions opposite each other. This was accomplished by remounting the flange containing the various angled detecting parts on the opposite side of the focus enclosure (See Figure 4-4-1). The results of these measurements show the same general behaviour as shown in Table 4-4. The strongest intensity was observed at  $0^\circ$  while the smallest intensity was at  $83^\circ$ . The complete understanding of the origin of the pattern of this radiation is not yet in hand, however, one which we believe to be making a significant contribution to the intensity distribution is described in the following paragraphs.

Assuming that the radiation originates from plasma bremsstrahlung, the power radiated per solid angle when the particle acceleration is  $\vec{a}$  is:

$$\frac{dP}{d\Omega} = A \int |\vec{n} \times (\vec{n} \times \vec{a})|^2 d^3x \quad (4-4-1)$$



SCHEMATIC OF ANGULAR DISTRIBUTION  
MEASUREMENT.

FIG 4-4-1

$\theta$	$0^\circ$	$55^\circ$	$68^\circ$	$83^\circ$
$\frac{I_\theta}{I_0}$	1	.37	.36	.22

$\theta$	$0^\circ$	$-55^\circ$	$-68^\circ$	$-83^\circ$
$\frac{I_\theta}{I_0}$	1	.35	.31	.19

X RAY INTENSITY ANGULAR  
DISTRIBUTION

TABLE 4 - 4

Where  $\vec{n}$  is a unit vector directed from the particle to the observer and A is a constant. The volume of integration includes the whole region of the plasma source. During collapse the plasma predominantly experiences a radial acceleration  $a_r$ . To consider the effect of this acceleration Eq. 4-4-1 is written in cylindrical coordinate as:

$$\frac{dP}{d\Omega} = A a_r^2 \int |\vec{n} \times (\vec{n} \times \hat{r})|^2 r dr d\theta dz \quad (4-4-2)$$

where  $\hat{r}$  is the unit vector in the radial direction.

The dimensions of the plasma are much smaller than the distance between the focus and the observer; we can neglect variations in  $\vec{n}$  over the source and express eq. (4-4-2) as:

$$I(\theta) = \frac{dP}{d\Omega} = B [1 + \cos^2 \theta] \quad (4-4-3)$$

Thus, one should expect the maximum at  $0^\circ$  and one half of the maximum at  $90^\circ$ . If we plot the intensity ratio  $I(\theta)/I(0)$  vs  $\frac{1}{2}(1 + \cos^2 \theta)$  the data of Table (4-4) appears in Figure 4-4-2.

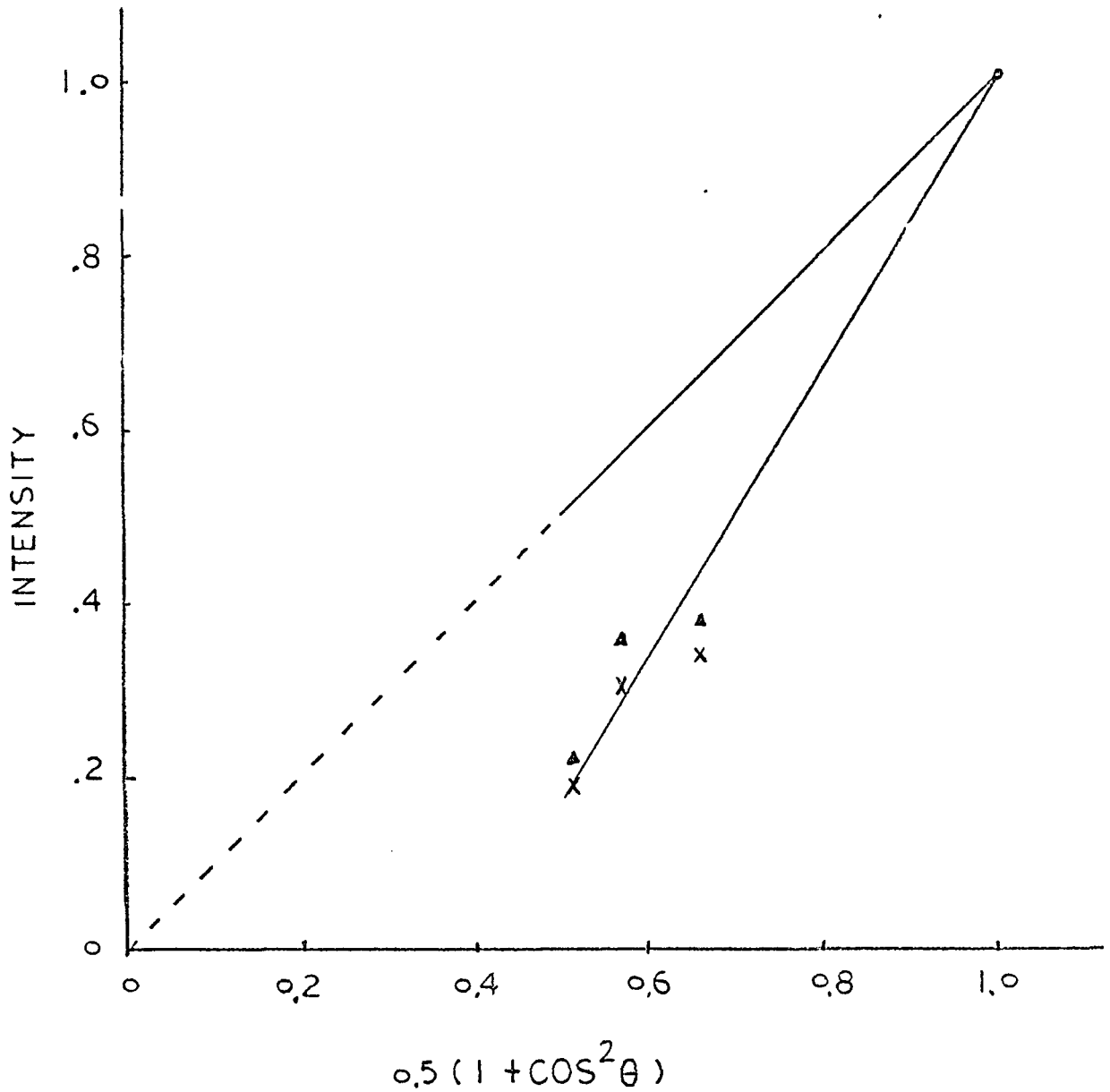
The apparent inconsistency between the theoretical and experimental results indicate some other effect should also play an important role, such as the electrode surface radiation. The x-rays generated by the electron bombardment of the electrode surface will propagate the distance  $d \sec \theta$  before coming out of the electrode surface, where d is the distance that bombarding electrons penetrated into the electrode surface. The intensity and the angular distribution of the x-rays originated from the surface radiation is dependant upon the energy distribution of the electrons and the geometric surface shape of the electrode.

Although the x-ray bremsstrahlung and line radiation from a thermal

75

▲ :  $\theta > 0$

x :  $\theta < 0$



X RAY INTENSITY ANGULAR  
DISTRIBUTION

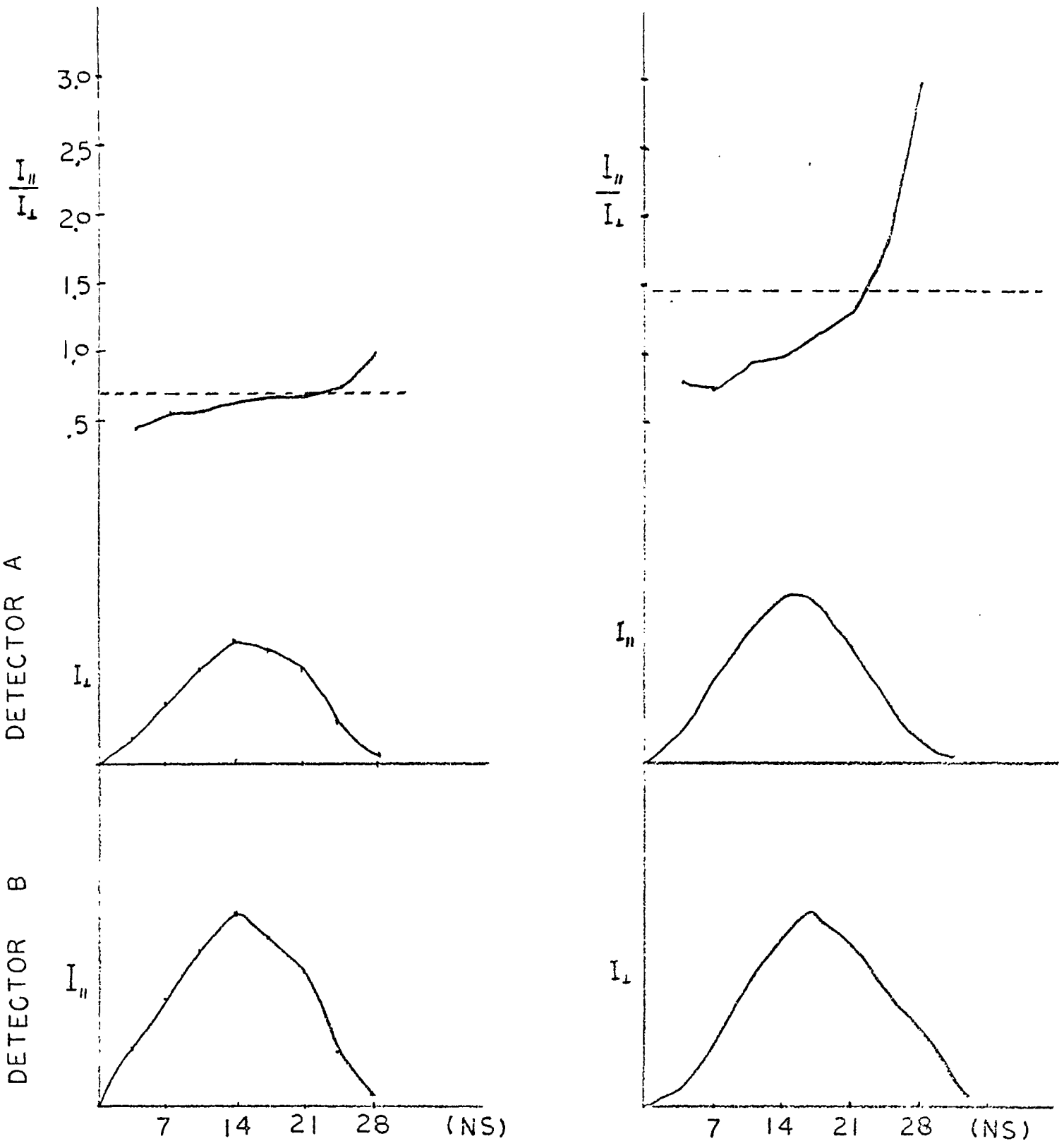
FIG 4-4-2

source should be unpolarized any asymmetry in the velocity distribution could lead to a partial polarization. Such asymmetry could exist both in the collapse phase and the subsequent turbulence phase. For this reason, there is considerable interest in examining the polarization of the x-ray emission.

The polarimeter used in this experiment is the one previously described. The polarimeter was used in the  $83^\circ$  position, which was as close to  $90^\circ$  as we could place it conveniently. The polarimeter was set to detect polarization along  $\Upsilon$  and  $Z$  directions.

Since the focus is in rapid dynamic change, we need to analyze the polarization as a function of time during the x-ray pulse.

The signals from the two detectors were displayed on the Textronik 551 oscilloscope on a 200 nsec/cm sweep. The polaroid picture of these traces were measured by using a power 12 microscope equipped with an ocular micrometer. The results obtained are shown in Figure 4-4-3. Figure 4-4-3a is the reconstructed signal from  $I_{\perp}$  while Figure 4-4-3b is the reconstructed signal from  $I_{\parallel}$ ; where  $I_{\perp}$  and  $I_{\parallel}$  represent the measured intensities of the scattered x-rays in the direction perpendicular and parallel to the DPF axis respectively. The ratio  $I_{\parallel} / I_{\perp}$  is plotted in Figure 4-4-3c. The polarimeter was rotated through  $90^\circ$  along its viewing axis, (See Figure 4-4-4) thereby interchanging the polarization seen by each detector. Figure 4-4-3d is the reconstructed signal from  $I_{\perp}$  while Figure 4-4-3e is the reconstructed signal from  $I_{\parallel}$  and Figure 4-4-3f is the ratio  $I_{\parallel} / I_{\perp}$ . If the x-rays generated by the DPF machine were polarized in the direction parallel to its axis the intensities of x-rays in Figure 4-4-3d



1ST DISCHARGE

2ND DISCHARGE

FIG 4-4-3 ILLUSTRATION OF POLARIZATION TIME VARIATION

should be small, and the intensities of x-rays in Figure 4-4-3b and Figure 4-4-3e should be large; however, if the x-rays were polarized in the direction perpendicular to the PDF axis the intensities in Figure 4-4-3a and Figure 4-4-3d should be large, and the intensities in Figure 4-4-3b and Figure 4-4-3e should be small.

Since the sensitivities of the detectors were not the same and the lithium scatterer was not scattering the x-rays isotropically, the intensity ratio of the two signals can not be used alone to signify the presence or absence of the polarization. However a change in the ratio of the signals with time would indicate a change of polarization.

If we assume that the detector parallel to the DPF axis has a sensitivity  $s_1$  and the fraction of x-rays scattered by the lithium scatterer in that direction is  $f_1$ , then, the measured intensity at this direction can be expressed as  $I_{||} = I_0 \cdot s_1 \cdot f_1$  where  $I_0$  is the intensity of the incident beam. Similarly, the measured intensity at the direction perpendicular to the DPF axis can be written as  $I_{\perp} = I_0 \cdot s_2 \cdot f_2$ , where  $s_2$  is the sensitivity of the detector perpendicular to the DPF axis and  $f_2$  is the fraction of x rays scattered by the lithium in that direction. The magnitude of both  $f_1$  and  $f_2$  depend on the polarization of the x ray source.

The ratio of the intensities at these two direction is simply  $I_{||} / I_{\perp} = s_1 f_1 / s_2 f_2$ . If we can assume that the detector's sensitivities are constants within the duration of the x ray emission, the ratio can be further simplified as  $I_{||} / I_{\perp} = A f_1 / f_2$  where  $A$  is a constant.

If the x ray source is unpolarized, or if the value of polarization is constant, the ratio  $f_1/f_2$  will be a constant during that period.

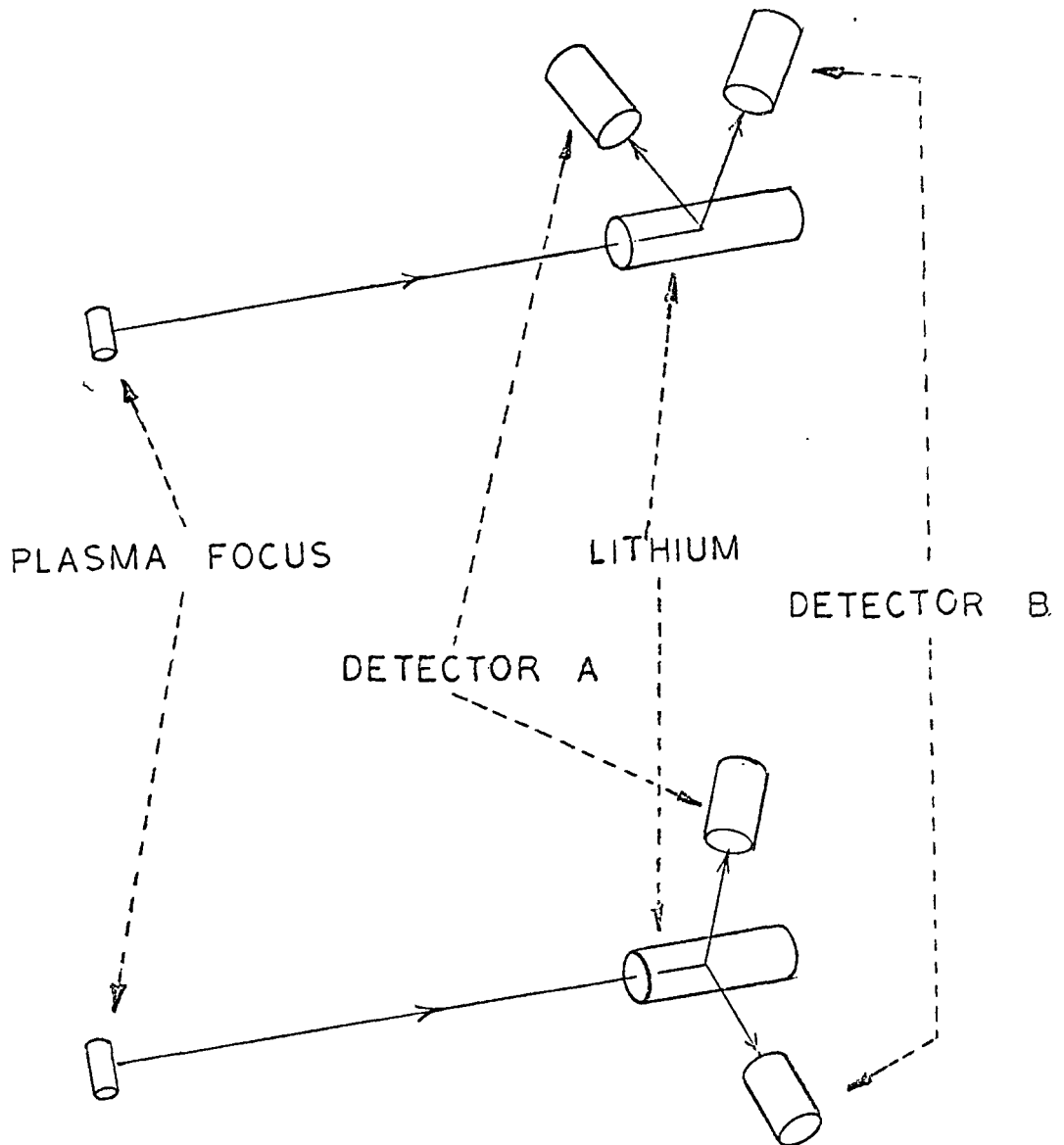


FIG 4-4-4 POSITIONS OF THE TWO DETECTORS BETWEEN THE DISCHARGES

However, if the polarization of the source is changing,  $f_1/f_2$  will change correspondingly and leads to the changing of  $I_{||}/I_{\perp}$ . Based on the analysis given in section 3-4, the monotonically increase of the ratio  $I_{||}/I_{\perp}$  is consistent with the model that the particles' acceleration change from an initial radial direction to an axial direction. This result leads to the idea that the plasma impinges radially to form the high density column but this initial radial collapse is not followed by a high velocity radial bounce. The density decay predominately through an axial flow and was believed to be away from the electrode. This picture is the same as that developed by analyzing hydrogen and deuterium plasma.<sup>(23)</sup> It appears that argon plasma behaves in a similar fashion.

Although the monotonically increasing of the ratio  $I_{||}/I_{\perp}$  are typical for many shots, polarization is observed in only about half the discharges. Data which appear to show no polarization is shown in Figure 4-4-5 where the analysis is similar to that used in Figure 4-4-3. These unpolarization radiation are believed as a result of un-symmetric collapse of the current sheath.

#### 4-5 X-Ray Spectrum Study

The x-ray energy spectrum of DPF has been determined by using a crystal spectrometer to measure the relative intensity of the continuous radiation at 4.96 keV, 8.6 keV and 11.5 keV.

In order to minimize variations which occurred from shot to shot, it was necessary to measure the incident beam and the diffracted beam at the same time. Two PIN detectors were used, the first measuring the scattered intensity while the second was used to monitor the intensity

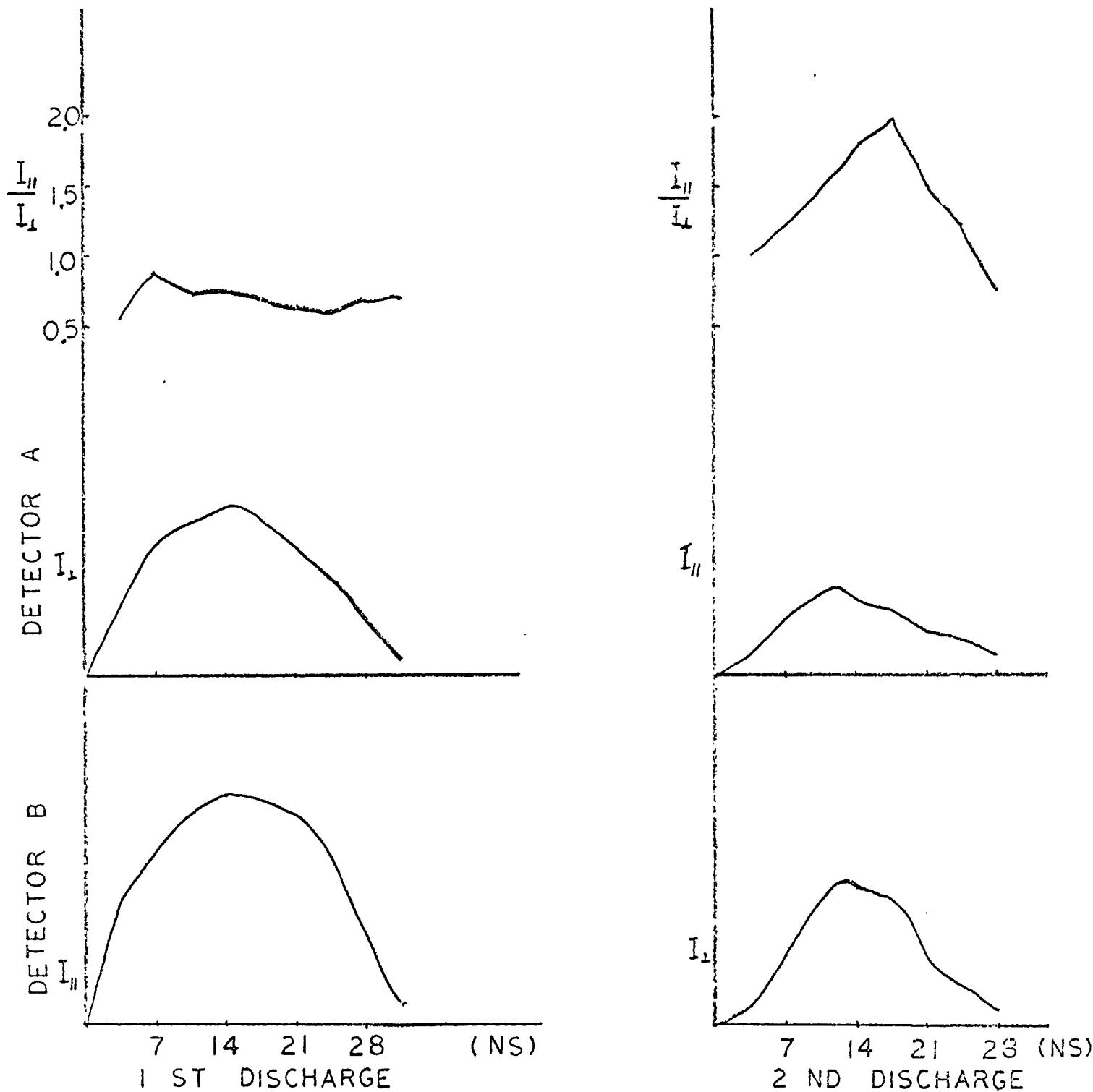
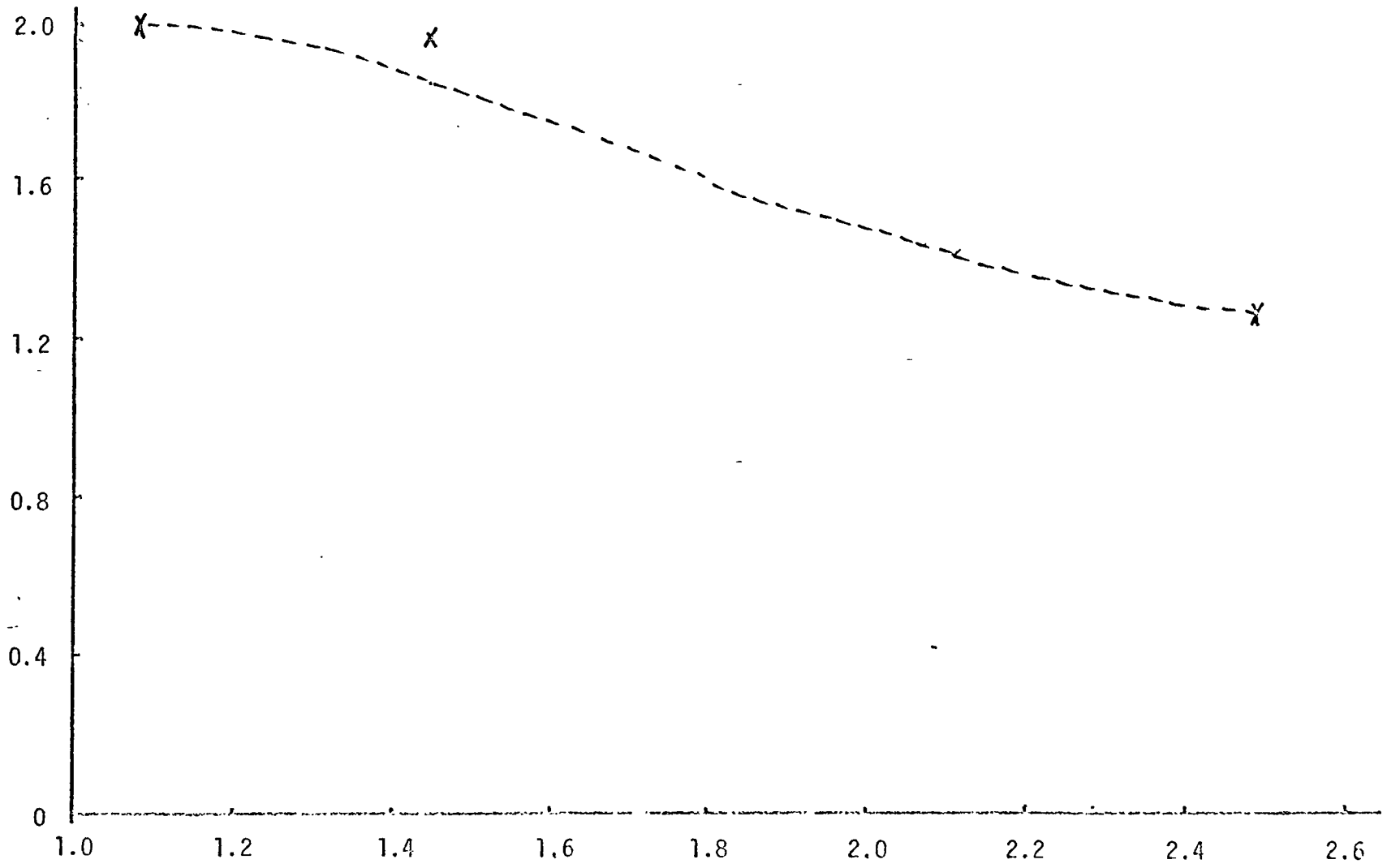


FIG 4-4-5 ILLUSTRATION OF POLARIZATION TIME VARIATION

of the x-ray source. The ratio of the scattered intensity to the source intensity was calculated for every discharge, and this value was multiplied by the reciprocal of the reflectivity of the crystal to obtain some value proportional to the relative power emitted in a particular energy range by the focus. The spectrometer was aligned to view the plasma from an angle of  $68^\circ$  measured from DPF axis. The x-rays seen by the spectrometer originated from both the electrode surface and the plasma column.

The PIN detector was set in the spectrometer at a position which satisfied the Bragg condition for x-rays of a given energy. However, the alignment was uncertain because of the variation in position of the plasma and the crudeness of the spectrometer. Therefore, the scattered intensities were measured for small changes in orientations of the crystal about the Bragg angle. The x-ray intensity at a specified wave-length was taken as the maximum observed scattered ratio, as the crystal orientation was moved about this angle. The results obtained following the above procedure are shown in Figure 4-5-1 where the intensity in a given wave-length band is plotted against wavelength. The dotted line corresponds to the bremsstrahlung spectrum emitted from a Maxwellian plasma with energy of approximately 6 keV.

The 6 keV plasma temperature is too high when compared with the 3 keV as estimated from the x ray pinhole picture. However, this controversy can be understood that the spectrum determined by the spectrometer was a composite of two sources, namely, plasma bremsstrahlung and the electrode surface radiation. Therefore, the different of 6 keV and 3 keV spectrum should be associated with the electrode surface radiation.



COMPOSED SPECTRUM FROM SURFACE RADIATION AND  
PLASMA BREMSSTRAHLUNG

FIG 4-5-1

The intensity ratio of the 6 keV plasma bremsstrahlung emitted at  $\lambda = 1.07 \text{ \AA}$  to that emitted at  $\lambda = 2.5 \text{ \AA}$  is 1.8 while the same ratio calculated for 3 keV plasma will be 0.59. If  $I_T(\lambda)$  is the spectrum of the x-rays generated from the target, then the relation:

$$\frac{1.8 - I_T(1.07)}{1 - I_T(2.5)} = 0.59 \quad (4-5-1)$$

must hold.

Assuming that the radiation generated from the electrode surface is thick target bremsstrahlung, its spectrum from a monoenergetic electron beam is: (27)

$$I_T(\lambda) = \frac{c'}{\lambda^2} \left( E - \frac{hc}{\lambda} \right) \quad (4-5-2)$$

where  $c'$  is a constant and  $E$  is the energy of the electron beam. Based on the intensity seen for different regions in the x-ray pinhole picture, the intensity of the 5 keV x rays emitted from the whole electrode surface was estimated about 3/10 of that emitted from the plasma column. Therefore we have the relation:

$$0.3 = I_T(2.5) = \frac{c'}{(2.5)^2} (E - 4.96)$$

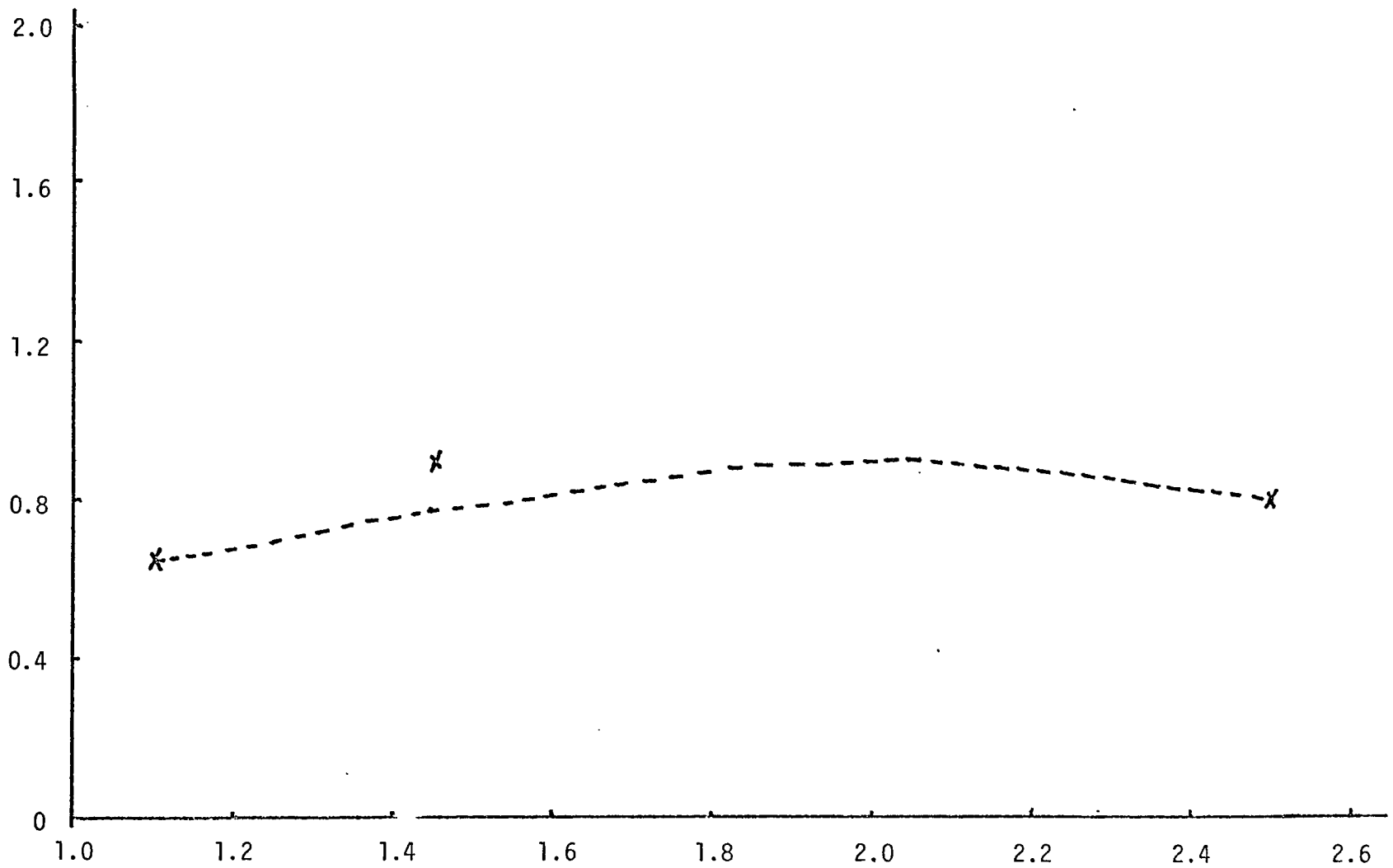
or

$$c' = \frac{1.875}{E - 4.96} \quad (4-5-3)$$

If one put this relation back into eq. (4-5-1) we have:

$$\frac{1.8 - \left( \frac{1.875}{E - 4.96} \right) \frac{E - 11.58}{(1.07)^2}}{0.7} = 0.59$$

on solving this equation for  $E$  we obtain  $E$  of approximately 48 keV.



SPECTRUM OF PLASMA BREMSSTRAHLUNG

FIG 4-5-2

We assume the spectrum observed by the spectrometer is composed of the radiation from the plasma focus as well as thick target bremsstrahlung emission by a 48 keV electron beam bombarding the electrode surface. The spectrum of the plasma column can be obtained by subtracting the thick target bremsstrahlung generated from 48 keV electrons from the measured spectrum. If we further assume that the intensity of the thick target bremsstrahlung at 5 keV is 3/10 of that generated by the plasma focus at the same energy we can obtain the spectrum of the plasma alone and this is shown in Figure 4-5-2. The dotted line is the bremsstrahlung spectrum for a 3 keV plasma. These 48 keV electrons are accelerated by the electric field in the direction pointing away from the electrode surface, and is consistent with Gary's theory.

#### 4-6 Conclusion

Based upon the series of experiments we have done on the argon filled DPF machine, we can reach the following conclusions:

A focus can be formed using argon gas. Although it has not been possible to achieve a focus with as much energy input as can be put into a hydrogen focus, the argon focus even at low energies is a more intense source of x rays. A better understanding of the physics of the argon focus will help us scale it to a higher energy, thereby obtaining an imposing pulsed source for x ray production. The following model appears to describe the dynamics of the focus.

At the initial focus stage, the density of the plasma increases from  $10^{18} \text{ cm}^{-3}$  to  $10^{19} \text{ cm}^{-3}$  within about 15 nsec. The radiation is generated by collision between radially decelerated electrons and ions,

and the resulting Bremsstrahlung is partially polarized. Based on the pin hole picture the temperature of the electrons is about 3 keV.

Following the maximum compression,  $m = 0$  instability will develop. The plasma focus expands across the magnetic field, and the magnetic field will diffuse into the plasma column. The motion of the B field generated an E field producing relative drift between electrons and ions. The electric field can heat the electrons more effectively than the ions, thereby making  $T_e / T_i > 1$ . The ion-acoustic wave become unstable and grow, leading to the appearance of anomalous resistivity which in turn causes the voltage across the column to rise. Ohmic heating through the anomalous resistivity leads to greatly increased heating of the plasma and the temperature goes to about 10 keV within 25 nsec.

The increase in plasma temperature will damp the instability leading to a reduction in resistivity. The induced E field generates a strong axial drift and the radiation generated by collision between axial decelerated electrons and ions is partially polarized in the axial direction. Approximately 55 nsec after the peak x ray emission, the resistivity becomes negligibly small and the heating becomes insignificant.

## REFERENCES

1. J. W. Mather; Methods of Experimental Physics, Vol. 9B, Academic Press. New York 1971.
2. N. V. Filippov, T. I. Filippova, V. P. Vinogradov; Nucl. Fusion Suppl. Pt. 2, 577 (1962).
3. J. W. Mather; Bull. Am. Phys. Soc. 8, 177 (1963).
4. J. Marshall; Physics Fluid 3, 134 (1960).
5. J. E. Osher; Physics Review Letter 8, 305 (1962).
6. M. Rosenbluth, R. Garwin; Los Alamo Sci. Lab Rep. LA-1850 Los Alamos Sci Lab. Los Alamos, New Mexico, (1954).
7. J. W. Mather; Plasma Physics Contr. Nuclear Fusion Res. Proc. Conf. 2nd 1965, 2, IAEA, Vienna 1966.
8. Ch. Maissonier, F. Pecorella, J. P. Rager, M. Samuelli; 2nd Topical Conf. on Pulsed High-Beta Plasmas, Garching (1972).
9. R. S. Post; Ph.D. Thesis, Infrared Emission and 10.6 Laser Scattering From the Dense Plasma Focus, 1973 Columbia University Press.
10. D. E. Potter; Physics Fluid 14, 1911 (1971).
11. M. J. Bernstein, D. A. Meskan, H. L. Van Paassen; Physics Fluid, 10, 2193 (1969).
12. Melvin Bernstein; The Review of Scientific Instruments, Vol 43 No. 9 1972.
13. M. J. Bernstein, D. A. Meskan, H. L. L. Paassen, Physics Fluid 12, 2193 (1969).
14. S. P. Gary, F. Hohl; Physics Fluid 16, 997 (1973).
15. C. E. Newman, V. Petrosian, Physics Fluid 18, 547 (1975).
16. V. A. Gribkov et al: JETP Letters 15, 329 (1972).
17. R. K. Landshoff; Magnetohydrodynamics, Stanford University Press (1960).

18. Krall and Trivelpiece; Principles of Plasma Physics, McGraw Hill (1973).
19. Melvin Bernstein; The Review of Scientific Instruments 43 1323 (1972).
20. I. P. Tindo, V. D. Ivanov, S. L. Mandel'stam and A. I. Shoryghin; Solar Physics 14, 204 (1970).
21. J. R. P. Angel, R. Novick, P. Vandebout and R. Wolff; Physical Review Letters 22, 861 (1969).
22. N. G. Alexandropoulos, J. Felsteiner and G. Cohen; To be published.
23. J. Dowing; Ph.D. Thesis The Dynamics of the DPF as determined from an Analysis of laser Scattering Spectrum 1973, University of Houston.
24. R. C. Elton, A. D. Anderson; Naval Research Laboratory, NRL Report 6541 (1967).
25. Cambel; Plasma Physics and Magneto Fluid Mechanics; McGraw Hill (1963).
26. Jackson; Classical Electrodynamics, Wiley (1965).
27. Kulenkampff, H. and L. Schmidt; Ann der Phys, 43 494 (1943).